The Coalescence Behavior of Two-dimensional Materials Revealed by Multi-scale *in situ* Imaging during Chemical Vapor Deposition Growth

Zhu-Jun Wang[1,2‡]*, Jichen Dong[3,‡], Linfei Li[4‡], Guocai Dong[5], Yi Cui[6], Yang Yang[7], Wei Wei[6,7],

Raoul Blume[2], Qing Li[8], Li Wang[9], Xiaozhi Xu[9], Kaihui Liu[9], Cédric Barroo[10], Joost W. M.

Frenken[5], Qiang Fu[7], Xinhe Bao[7], Robert Schloegl[2], Feng Ding[3]*, Marc-Georg Willinger[1,2,11]*

‡These authors contribute equally to this work

*Corresponding authors: zhujun.wang@scopem.ethz.ch, f.ding@unist.ac.kr, marc.willinger@scopem.ethz.ch

1. Scientific Center for Optical and Electron Microscopy, ETH Zürich, 8093 Zürich, Switzerland
2. Department of Inorganic Chemistry, Fritz Haber Institute of the Max Planck Society, Berlin-Dahlem D-14195, Germany
3. School of Materials Science and Engineering, and Department of Chemistry, Ulsan National Institute of Science and Technology (UNIST), Ulsan 44919, Republic of Korea
4. Department of Chemistry, University of Illinois at Chicago, Chicago, Illinois 60607, United States
5. Kamerlingh Onnes Laboratory, Leiden University, P.O. Box 9504, 2300 RA Leiden, Netherlands
6. Vacuum Interconnected Nanotech Workstation, Suzhou Institute of Nano-Tech and Nano-Bionics, Chinese Academy of Sciences, Suzhou 215123, China
7. State Key Laboratory of Catalysis, Dalian Institute of Chemical Physics, Chinese Academy of Sciences, Dalian 116023, China
8. Institute of Functional Nano & Soft Materials (FUNSOM), Collaborative Innovation Center of Suzhou Nano Science and Technology, Soochow University, Suzhou 215123, Jiangsu, China
9. State Key Laboratory for Mesoscopic Physics, Collaborative Innovation Centre of Quantum Matter, School of Physics, Peking University, Beijing 100871, China
10. Chemical Physics of Materials and Catalysis, Faculty of Sciences, Université Libre de Bruxelles, CP243, 1050 Brussels, Belgium
11. Department of Colloid Chemistry, Max Planck Institute of Colloids and Interfaces, Potsdam, D-14424, Germany

ABSTRACT

Wafer-scale monocrystalline two-dimensional (2D) materials can theoretically be grown by seamless coalescence of individual domains into a large single-crystal. Here we present a concise study of the coalescence behavior of crystalline 2D films using a combination of complementary *in situ* methods. Direct observation of overlayer growth from the atomic to the mm-scale and under model- and industrially relevant growth conditions reveals the influence of the film-substrate interaction on the crystallinity of the 2D film. In the case of weakly interacting substrates, the coalescence behavior is dictated by the inherent growth kinetics of the 2D film. It is shown that the merging of co-aligned domains leads to a distinct modification of the growth dynamics through the formation of fast-growing high-energy edges. The latter can be traced down to a reduced kink-creation energy at the interface between well-aligned domains. In the case of strongly interacting substrates, the lattice mismatch between film and substrate induces a pronounced Moiré corrugation that determines the growth and coalescence behavior. It furthermore imposes additional criteria for seamless coalescence and determines the structure of grain boundaries. The experimental findings, obtained here for the case of graphene, are confirmed by theory-based growth simulations and can be generalized to other 2D materials that show 3- or 6-fold symmetry. Based on the gained understanding of the relation between film–substrate interaction, shape evolution and coalescence behavior, conditions for seamless coalescence and thus, for the optimization of large-scale production of monocrystalline 2D materials, are established.

KEYWORDS

multi-scale *in situ* imaging, seamless coalescence, 2D materials, complementary *in situ* methods, chemical vapor deposition, pressure-gap

Large-scale application of two-dimensional (2D) materials in technology will only be possible once industrial scale fabrication of high quality, single-crystalline films becomes really feasible.[1-3] Currently, chemical vapor deposition (CVD) is the most widely used method to grow 2D films onto various substrates.[4-12] One promising strategy towards the fabrication of single-crystalline 2D films is based on the controlled coalescence of co-aligned domains into a continuous, grain boundary (GB)-free film.[13,14, 15] Despite recent achievements, the role of the substrate and growth conditions on the growth and coalescence behavior of 2D films is not sufficiently understood, and consequently, possibilities of "seamless stitching" not engaged.[16] Using graphene as a prototype material, we present here a detailed study on the effect of the film–substrate interaction on the growth and coalescence behavior and demonstrate that the key findings can be generalized to other 2D materials.

To get a better understanding of the conditions required for seamless coalescence, the parameters that determine the growth behavior must be studied in detail. *In situ* methods that enable direct visualization of crystal growth and evolution are ideally suited to study the growth kinetics of 2D materials.[7, 17-21] However, surface science imaging techniques, such as low-energy electron microscopy (LEEM),[7] photoemission electron microscopy (PEEM)[22] and scanning tunneling microscopy (STM)[23, 24] are designed to work under pressures that are up to 10 orders of magnitude lower than those encountered in practical CVD conditions.[14, 25, 26] This large pressure-gap raises the question about the transferability of growth mechanisms derived on the basis of (ultra-high vacuum) UHV observations to conditions applied in industrially relevant CVD processes.[27]

By using a combination of complementary *in situ* tools, we are able to monitor details of the growth- and coalescence behavior from the atomic to the millimeter scale and across the pressure gap between UHV and relevant CVD growth conditions. This unique combination of *in situ* real-space imaging and spectroscopic methods allows us to link atomistic details with macroscopic growth dynamics, including information about the chemical state. The results show that the coupling-strength between film and substrate does not only determine the growth behavior, but also dictates conditions for seamless coalescence. In the case of a weak coupling, coalescing domains are able to slightly slide and rotate, enabling seamless stitching and GB free merging without the requirement of perfect alignment. In the case of strongly coupling substrates, alternating adsorption sites induce a substantial periodic buckling in the form of a Moiré corrugation. In this case, seamless coalescence requires, in addition to a coinciding orientation of the 2D film lattice, a coherence of the Moiré corrugation of the respective domains. Using theoretical analysis based on density functional theory (DFT) simulations and kinetic Wulff constructions (KWC), we are able to fully describe the coalescence process and show how atomistic processes are expressed on the macroscopic level. Based on the fundamental understanding of the coalescence behavior at different length-scales, we present macroscopically observable growth features and shape evolution that can be used to identify GB-free coalescence. By extending the findings from graphene to other 2D films, we present a macroscopically observable criterion that can be used to identify GB-free coalescence in 2D materials that show 3- or 6-fold symmetry. Our findings thus set a general framework for the understanding of the role of film–substrate interactions during growth and provide guidelines for the controlled production of single crystalline 2D films.

RESULTS AND DISCUSSION

In order to study the influence of the film–substrate interactions on the growth and coalescence behavior, *in situ* growth experiments were performed on (111) surfaces of Pt and Rh.[28-30] The two substrates were chosen as representatives for materials that show a weak (Pt) and a strong coupling strength (Rh) with graphene, respectively.[31, 32]

Bridging the pressure gap from UHV to relevant CVD condition by multi-*in situ* approach

A set of complementary *in situ* imaging tools have been applied in order to trace effects related to the coupling strength from the atomic scale to the macroscopically observed growth behavior. Since these complementary *in situ* techniques operate at different pressures, we are able to bridge the pressure–gap from UHV to relevant CVD conditions. While *in situ* environmental scanning electron microscopy (ESEM) and LEEM allows for the direct observation of the growth dynamics under pressures ranging from $\sim 10^{-7}$ Pa to ~ 100 Pa at the micrometer to the nanometer length-scale,[33-37] *in/ex situ* STM provides details of graphene growth at the nanometer/atomic length-scale under UHV conditions.[23, 38] In the case of growth on Rh(111), our growth experiments showed that graphene islands are generally terminated by the most stable zigzag edges,[34, 39] and that the shape of single-crystalline graphene islands basically remains the same over the whole studied pressure range (**Figure 1 d, g, j**). Only in the case of growth at very low pressure ($\sim 10^{-7}$ Pa) and in the absence of H_2 (**Figure 1 a**), islands exhibit a lens-like shape, in agreement with previous observations.[7] Due to the strong graphene-substrate interactions, the domains are aligned to the Rh(111) surface under all observed pressure conditions, as confirmed by low energy electron diffraction (LEED) measurements of graphene grown inside the ESEM and LEEM chambers, respectively (see **Figure 1**).[40, 41] As a consequence, only one type of periodicity in the Moiré

pattern is observed. *In/ex situ* STM measurements of graphene grown in the ESEM/LEEM chamber show that the unit cell of the Moiré lattice measures approximately 2.9 nm (see the rhombuses drawn in **Figure 1c, f, i, l**) and is caused by the lattice mismatch between graphene (2.46 Å) and Rh(111) (2.69 Å).[23, 32, 42]

The chemical state of carbon during graphene formation on Rh(111) was monitored using *in situ* near ambient pressure X-ray photoelectron spectroscopy (NAP-XPS). The C_{1s} peak, which provides a chemical fingerprint of the carbon structure and is sensitive to changes in the graphene–substrate interaction,[36] was followed during growth under pressures ranging from $\sim 10^{-3}$ to 20 Pa (see **Figure 1 m-p**). For growth in pure C_2H_4 at 10^{-3}Pa, the C_{1s} spectrums exhibits two peaks centered at 284.72 and 284.3 eV, respectively. The two energetic positions reflect the modulation of the graphene-substrate interaction strength due to the Moiré corrugation (see STM in **Figure 1**).[31,43]

The composition of the C_{1s} signal is consistent across the observed pressure range and indicates that the stacking configuration and coupling-strength of graphene on Rh doesn't change within the observed pressure range.
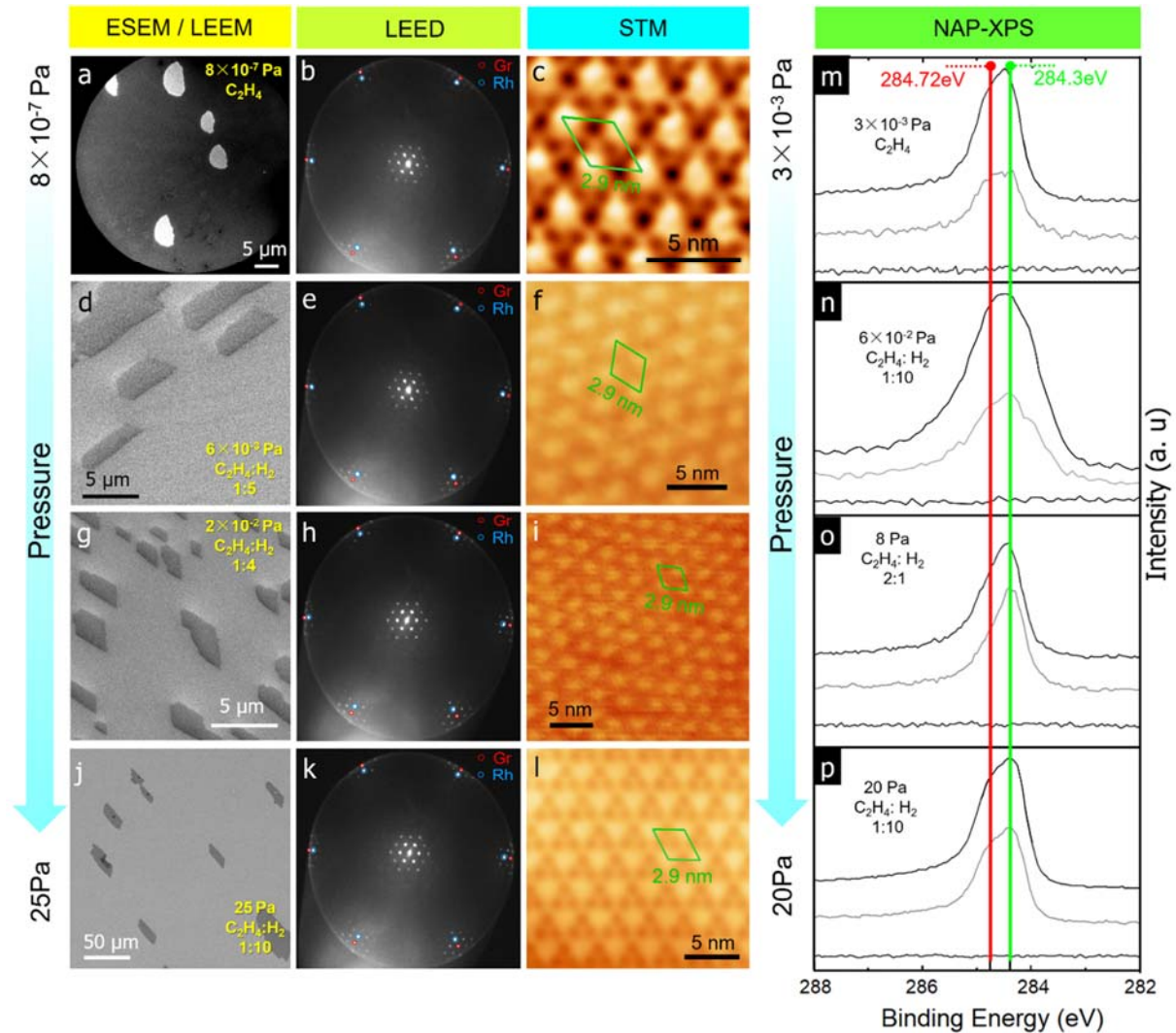
Figure 1. Graphene growth on Rh(111) under different pressure. (a, d, g, j) *In situ* LEEM/ESEM images obtained during growth of graphene domains by CVD from C_2H_4 on Rh(111) at constant temperature (T=900 °C). Growth condition (pressure, C_2H_4:H_2): (a) 8×10^{-7}Pa, pure C_2H_4; (d) 6×10^{-3}Pa, 1:5; (g) 2×10^{-2}Pa, 1:4 and (j) 25Pa, 1:10. The corresponding LEED patterns and STM images of graphene grown within the ESEM/LEEM chamber at different condition are shown in (b-c), (e-f), (h-i) and (k-l) respectively. In (b), (e) (h) and (k), the six inner diffraction spots (marked by blue circles) are from Rh(111), and the outer spots (marked by red circles) are from graphene. The green rhombuses in (c), (f), (i), and (l) indicate the $(12 \times 12)_C$ on $(11 \times 11)_{Rh}$ Moiré superstructure. (m-p) show C_{1s} spectra recorded during graphene growth on Rh(111) at 900 °C under different gas environments. (m) Exposure to pure C_2H_4 at 3×10^{-3} Pa; (n) Exposure to1:10 C_2H_4:H_2 gas mixture at 6×10^{-2} Pa; (o) Exposure to a 2:1 C_2H_4:H_2 gas mixture at 8 Pa; (p) Exposure to a 1:10 C_2H_4:H_2 gas mixture at 20 Pa; Binding energies of the main components were derived by spectral deconvolution and are indicated in the figure.

In the case of graphene growth on Pt, the extent to which the graphene-substrate interaction affects the growth depends weakly on the growth conditions. As shown in **Figure 2a,b,c**, growth under high vacuum ($\sim 10^{-6}$ Pa) and in the absence of hydrogen results in the presence of two different in-plane orientations. Consequently, the LEED patterns of graphene grown inside the LEEM chamber shows six spots due to the Pt(111) substrate (blue circles in **Figure 2b**), and two sets of six spots due to two sets of differently oriented graphene domains (highlighted as red and green circles in **Figure 2b**). The relative rotation angle between graphene domains and the substrate is either 19° (R19) or 11° (R11). These two orientations give rise to two distinct Moiré superstructures that are rotated with respect to one another by 21° (see **Figure 2b**). In agreement with a strain-driven model proposed by Merino *et al.*, the periods of these Moiré superstructures measure 0.74 nm (R19.1°) and 1.13 nm (R10.9°), respectively.[44] The STM measurements of graphene grown inside the LEEM chamber confirm the coexistence of these two types of Moiré patterns (**Figure 2c**). The different colored rhombus in the STM image (**Figure 2c**) highlight the two types of Moiré patterns, 1.1nm (R11°) and 0.74nm (R19°), with 21° rotation, in agreement with LEED observations (**Figure 2b**). Growth at slightly higher pressure ($\sim 10^{-3}$ to $\sim 10^{-2}$ Pa) and in the presence of H_2 and C_2H_4, results in the formation of only co-oriented graphene domains on Pt (see ESEM measurements in **Figure 2d, g**). LEED measurements (**Figure 2f, j**) show that the graphene lattice is rotated with respect to the Pt(111) by 19°. The dominance of only one orientation is a consequence of an increased nucleation barrier and the competition between hydrogen etching and growth in the presence of H_2. It reflects a slight difference in stability between the R19.1° and R10.9° configurations.[44, 45] Further increase of the H_2-C_2H_4 pressure to 25 Pa results in a higher growth rate. The slight energetic difference between different Moiré superstructures is no longer a discriminating factor for the selection of a dominant (low-energy) orientation of graphene

islands. As a consequence, domains with a wide variety of rotational Moiré variants can be observed by *in situ* ESEM/LEED/STM (**Figure 2j-l**). The dependence of the growth behavior on the growth conditions reflects the weak coupling strength on Pt and is in accordance with previous observations.[37, 46] However, except for the selection or preference of different rotational configurations, no influence of the growth conditions on the inherent growth behavior of graphene was found. Indeed, a comparison of the *in situ* ESEM/LEEM, LEED and STM data shows similar shape evolutions across the whole observed parameter space.

Again, the evolution of the C_{1s} peak was monitored during growth under different pressure and growth conditions by NAP-XPS in order to assess the influence of growth conditions on the chemical fingerprint of the formed graphene.

Growth at 3×10^{-3} Pa of C_2H_4 leads to a peak located at 284.76 eV with a shoulder at 285.2 eV. The latter can be assigned to the presence of sp^3-bonds (**Figure 2m**), either due to C-H bonds at graphene edges or due to defects that can exist on the edges or inside of the graphene plane. Defects are likely to be present due to the lack of H_2 etching during graphene growth.[47] By increasing the pressure to 2×10^{-2} Pa and adding H_2 into the chamber (*i.e.* under H_2-C_2H_4 gas mixtures), the dominance of the 284.76 eV component is maintained up to pressures of ~8 Pa (**Figure 2n, o**). Further pressure increase to 20 Pa induces a small shift of ~0.5 eV towards lower binding energy (**Figure2 p**). Here, the graphene growth starts with the appearance of a peak at 284.25 eV, which is shifted towards the peak at 284.68 eV with longer growth time (**Figure2 p**). We attribute the change in binding energy to the presence of randomly rotated graphene islands on Pt(111) based on the growth observed by *in situ* ESEM, LEED and STM (**Figure2 j-l**). Indeed, the substrate–overlayer interactions change with the rotational angle and is lower for randomly oriented islands.[44]

The *in situ* NAP-XPS experiments prove that a comparison between high vacuum *in situ* STM/LEEM and near-ambient pressure *in situ* ESEM is legitimate and that one can draw a consistent picture from UHV to relevant CVD conditions (**Figure1-2**).
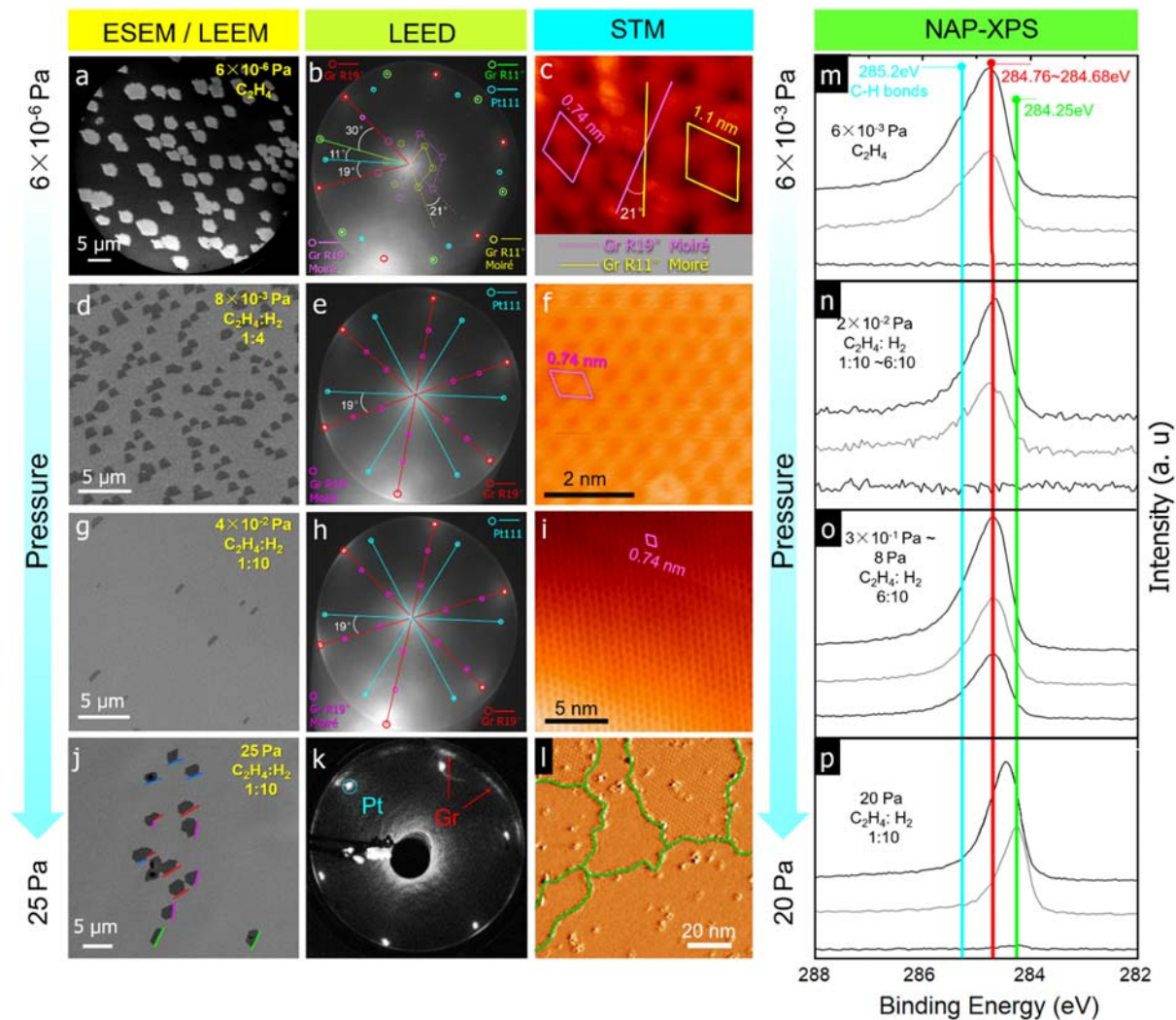

Figure 2. Graphene growth on Pt(111) under different pressure. (a, d, g, j) *In situ* LEEM/ESEM images obtained during growth of graphene domains by CVD from C_2H_4 on Pt(111) at constant temperature (T=900 °C). Edges of the graphene in (j) marked by the same colored lines are parallel with each other. Growth condition (pressure, C_2H_4:H_2): (a) 6×10^{-6}Pa, pure C_2H_4; (d) 8×10^{-3}Pa, 1:4; (g) 4×10^{-2}Pa, 1:10 and (j) 25Pa, 1:10. The corresponding LEED patterns and STM images of graphene grown within the ESEM/LEEM chamber at different condition are shown in (b-c), (e-f), (h-i) and (k-l) respectively. In (b), (e) and (h), the six inner diffraction spots (marked by blue

circles) are from Pt(111), and the outer spots (marked by red/green circles) are from graphene. The dots denoted by yellow and purple circles are from graphene/Pt(111) Moiré. The yellow rhombus in (c) indicate Moiré superstructure of R11° graphene. The purple rhombus in (f) and (1) indicate Moiré superstructure of R19° graphene. (m-p) C_{1s} spectra of graphene growth on Pt(111) recorded at 900°C under different gas environments. (m) Exposure to pure C_2H_4 at 6×10^{-3} Pa; (n) Exposure to C_2H_4:H_2 gas mixtures at 2×10^{-2} Pa with ratios between 1:10 to 6:10; (o) Exposure to a 6:10 C_2H_4:H_2 gas mixture at pressures between 3×10^{-1} and 8 Pa; (p) Exposure to a 1:10 C_2H_4:H_2 gas mixture at 20 Pa. Binding energies of the main components derived from a deconvolution procedure are indicated in panel m.

Coalescence and GB formation on weakly interacting substrates

The occurrence of graphene domains with different in-plane orientations offers a practical way to compare the coalescence behavior of aligned and misaligned domains under identical growth conditions.

We first analyze the case of misaligned domains:

Due to the six-fold symmetry of graphene, the rotational misalignment between adjacent grains can only vary between 0 and 30°. In **Figure 3a**, the 94° angle between the two zigzag edges at the concave corner shows that the neighboring domains are misaligned by 26°. The propagation of the adjacent growth fronts and, respectively, the trajectory of the concave corner is indicated by arrows and a dotted line in **Figure 3** (see also **Supporting Movie 1**). During the coalescence, the angle between the growth fronts remains unchanged (see **Figure 3a-c,** and **Supporting Movie 1**). The propagation of the concave corner during growth depicts the position of the resulting GB, as suggested by theory.[48] It can be visualized by simply switching from growth conditions to hydrogen etching. As shown in **Figure 3d-f** and **Supporting Movie 2**, exposure to pure hydrogen at 900 °C leads to preferential etching at defects and eventually, the formation of chain of vacancy islands that are terminated by zigzag edges.[47, 49, 50] The orientation and individual shape of the vacancy islands is shown in **Figure 3d-f**. The angles between the zigzag edges confirms that all the observed vacancy islands indeed originate from the line defined by the motion of the concave

corner (**Figure 3g-h**). It should be pointed out here that GBs between growing domains do not necessarily form straight lines.[13, 51] Slight variations in the growth speed of the respective edges can result in a curved GB (**Figure 3f**), in agreement with previous visualizations of GBs in CVD graphene.[52-56]
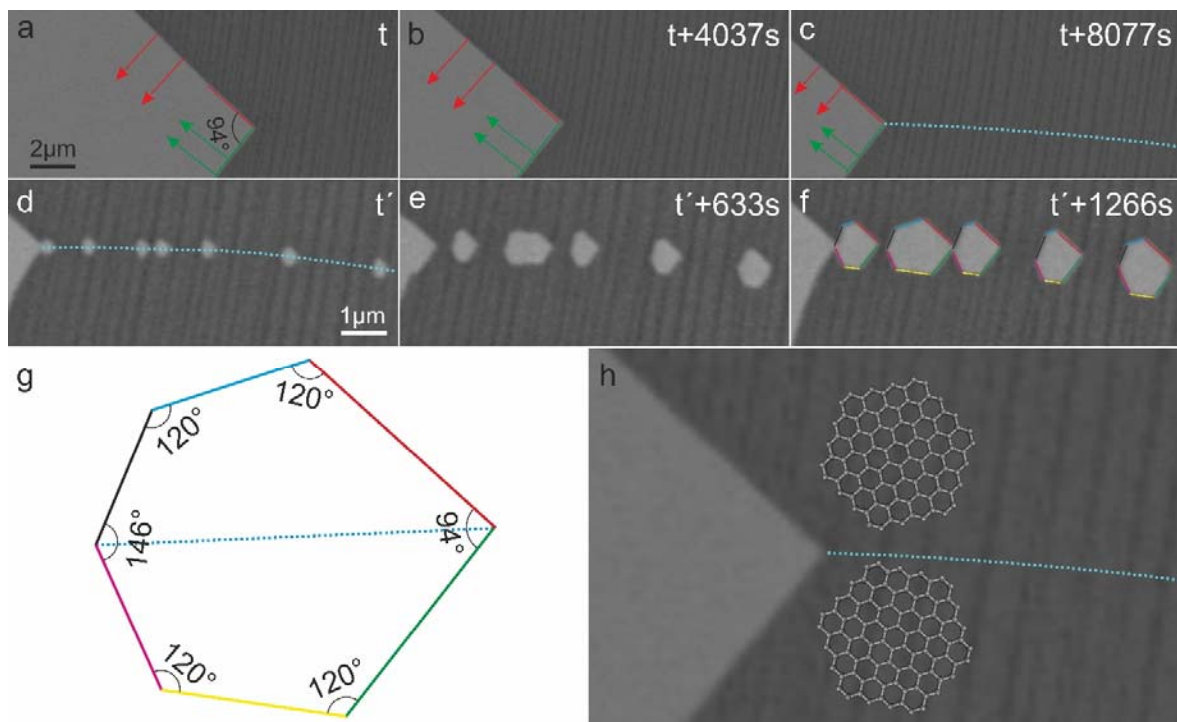

Figure 3. Identification of the graphene grain boundary and relative angle between adjacent grains by isothermal etching of vacancy islands on Pt(111). (a-c) *In situ* ESEM images of coalescing graphene domains at 900 °C showing the edge evolution at the concave corner of misaligned domains growing on Pt. The dashed line in (c) highlights the trajectory of the concave corner and maps the position of the GB. The arrows in (a-c) indicate the expansion direction of the zigzag terminated edges during growth. (d-f) Shape evolution of etching pits during subsequent H_2 etching at 900 °C. All the etching pits present a similar shape and appear along the GB (dashed line). Zigzag edges of the etching pits are marked by colored lines in (f). Each color represents a zigzag direction. The angular relation between edges of the etching pits is represented in (g). The respective honeycomb lattice of the two grains are indicated in (h). The induction time *t'* is needed to open a hole, *i.e.* initiate the etching process at the line defect in the polycrystalline graphene.

In the case of well-aligned domains, the concave angle between the respective zigzag growth fronts can only measure either 60 or 120°.[42] In the frame of our experiments, both cases have been observed (see **Figure 4** and **Supporting Movie 3**, and **Figure 5a,b**).

When two zigzag edges of aligned neighboring domains meet, fast attachment of growth species at the concave corner leads to the formation of new growth fronts. (**Figures 5c-f**). These growth fronts are tilted with respect to the zigzag edges by an angle of approximately 19° (**Figure 5e**). They expand rapidly and replace the original zigzag edges. Due to their high growth speed, they lead to a quick filling of the area between adjacent domains until either a straight zigzag edge or 120° vertexes between two zigzag edges is established (refer to corner highlighted by red lines in **Figure 4f** and **Figure 5b**).
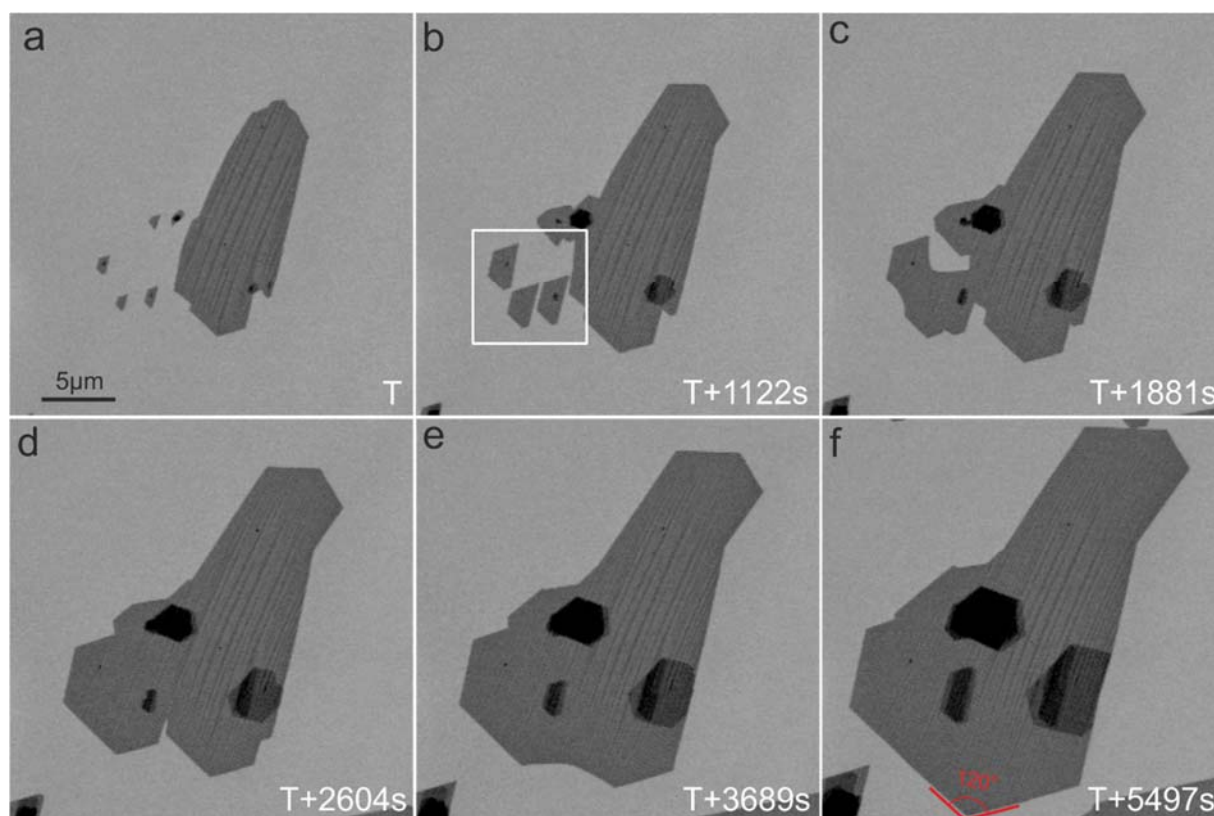

Figure 4. *In situ* ESEM images recorded at 900°C showing the nucleation and coalescence of graphene on Pt(111) at different growing time. The growing graphene sheets are characterized by

a dark contrast. The domains enclosed by a white rectangle in (b) show a slight misalignment (a magnified image showing the misalignment is presented in **Figure SI 4**).

In order to rationalize the experimental findings, we first recall that the growth rate along different directions depends on the energy of the respective edge and is determined by the concentration of kinks.[50] Kink-creation, which is the rate-limiting step during growth, should be energetically favorable at the concave corner if the adjacent domains are well-aligned.[42] Fast creation of new kinks at the concave corner is presumably the reason for the observed smoothening of the concave corner and formation of the fast growing edge (see **Figure 5a,c-f**).

In order to confirm that the fast growth at the concave corner between well-aligned domains is due to a reduced kink-creation energy, we performed KWC simulations the shape evolution (refer to **Supporting Note 1**).[57] **Figure 5g-k** shows the simulated growth process at the concave corner between well-aligned domains for the case of domains that coalesce from different directions and present concave corners of either 120° (**Figure 5h**) or 60° (**Figure 5i-k**). For the simulation, hexagonal shaped graphene domains were used, although experimentally observed domains generally deviate from ideal hexagons due to growth speed modulation by steps on the substrate surface. Due to the hexagonal geometry of the honeycomb lattice of graphene, the formation of kinks is easiest at concave corners presenting an angle of 60° or 120°, as confirmed by DFT simulations (refer to **Supporting Note 2**).

After attachment of carbon atoms at the concave corner, a sequence of new low-energy attachment sites is generated, as shown in **Figure 5g**. The sequential filling of low-energy sites leads to the formation of a new growth edge. This edge is tilted with respect to the zigzag edge by approximately 19.1°. It is characterized by having the highest possible kink density and is thus the fastest growing edge during attachment limited growth. The simulations clearly show that the

sequence of preferential attachment is the explanation for the observed rounding of the concave corner during the coalescence of aligned domains. Since the conditions for the formation of a 19.1° edge are only met if the carbon rings at the concave corner are not distorted, their appearance can be used to identify GB-free coalescence.
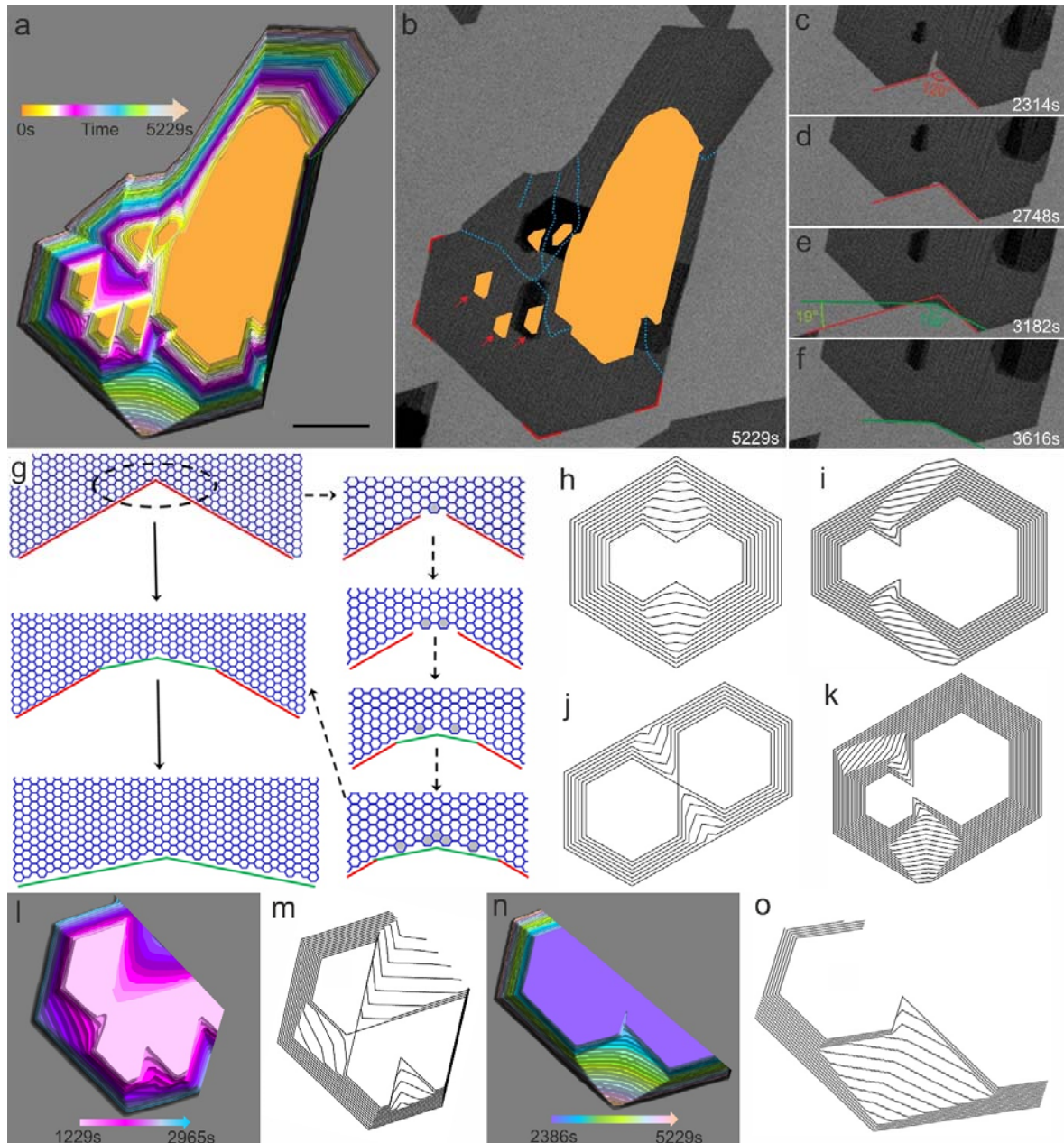

Figure 5. ESEM imaging of graphene growth on Pt(111) at 900 °C and KWC simulation of the shape evolution during the coalescence process. (a) Shape evolution of the graphene domains

during coalescence, reproduced as color-coded superposition of outlines that were abstracted from images recorded during a 5300 s interval (**Supporting Movie 3**). The scale bar measures 5 μm. (b) Representation of the graphene GBs after coalescence. The blue dashed lines in (a) and (b) indicate the motion trajectory of the intersection point of misaligned graphene domains, which are responsible for GB formation during coalescence. The orange color-coded domains in (b) highlight the shape of graphene at the beginning of the recording. (c-f) Sequence of images showing the apparition of new edges at the concave corner during coalescence (the initial angle of the concave corner is highlighted by red lines, whether the new edge angle is depicted in green). (g) Atomistic model of the growth process of a concave corner with an angle of 120° and zigzag edges in the case of well-aligned graphene domains. (h-k) KWC simulation of the shape evolution of well-aligned domains that coalesce from different directions and present concave corner with an angle of either 120° (h) or 60° (i-k). (l) Superposition capturing the area of coalescence from three aligned domains marked by red arrows in (b). The outlines of growing domain are color-coded according to the growth time provided in the color legend. (n) Shape evolution of the graphene, reproduced as color-coded superposition of outlines that were abstracted from a sequence of *in situ* ESEM images (c-f). The corresponding coalescing processes shown in (l) and (n) are simulated by our modified KWC and presented in (m) and (o).

To validate the above discussion, we performed additional KWC simulations in order to reproduce the experimentally observed shape evolution of coalescing graphene domains (refer to **Supporting Note 3** for simulation details).[57] A single frame from the *in situ* recorded movie was used as starting point (**Figure 5l, n**). Besides the shape and position of the initial domains, only the growth speed of the zigzag edges was used as parameters for the simulation of the coalescence behavior. (The growth rate profile is provided in **Figure SI 3**).

The striking consistency between the experimental coalescence of well-aligned graphene and the simulated evolution validates our above proposed coalescence mechanism.

One notable point is that the appearance of 19.1° edges at the concave corner does in fact not require a perfect alignment between the coalescing domains. As exemplified in the area marked by a white square in **Figure 4b** and **Figure SI 4**, we observe that the growth behavior of graphene domains follows that of well-aligned grains during merging as long as the angle of misalignment is less than ~3°. We assume that the in-plane strain, which is generated during the coalescence, induces a correction of the misalignment through a slight rotation of one of the domains. Indeed,

graphene rotation has been observed on other weak interaction substrate during annealing at growth temperature.[58] Alternatively, during coalescence, the in-plane strain can induce a continuous rearrangement of the graphene lattice at the GB in order to decrease the orientation-dependent energy.[59] In this case, the GB will be pushed through the grain with the higher energy. The misaligned grain thus in effect shrinks during the coalescence process.

It should be mentioned here that there are cases, in which the 19.1° edges do not evolve, even though two grains are perfectly co-oriented.[60-63] One such case is shown in **Figure 6**. Close inspection by real-time imaging revealed that the attachment of carbon atoms at the concave corner is prevented by a surface impurity (see highlighted by red arrow in **Figure 6**). This observation does not only highlight the importance of growing on surfaces that are free of impurities, but also provides an indirect proof that the kink creation at the concave corner is responsible for the formation of the 19.1° edge. Finally, this also further validates the rationalities and efficiencies of the theoretical model.
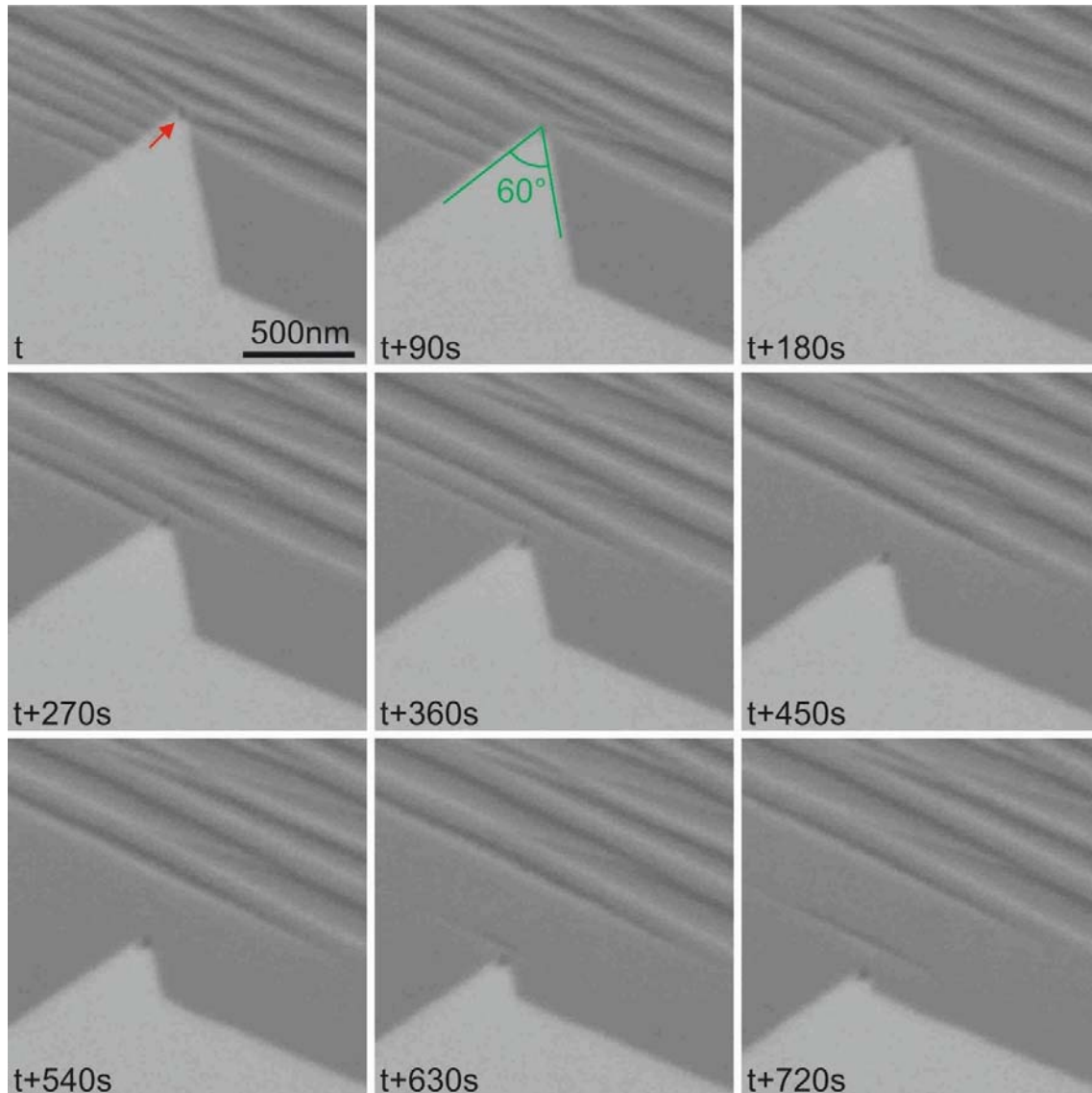
Figure 6. Time-lapse image series recorded during the coalescence of well-aligned domains on Pt(111) at 900 °C. The surface impurity, depicted by a red arrow in the first panel, disturbs the attachment of C adatoms at the 60° concave corner and thus, the development of the 19.1° edges.

Coalescence and GB formation on strongly interacting substrates

In the case of a strong film–substrate interaction, the graphene layer will present a preferential in-plane orientation. Unlike the coalescence behavior on Pt, the most distinctive feature of graphene coalescence on Rh is that, even though the domains are well-aligned, the characteristic

formation of 19.1° edges is not observed at the concave corner during coalescence. Instead, the angle of the concave corner remains unchanged with a value of 120° or 60° (**Figure 7** and **Supporting Movie 4-5**).
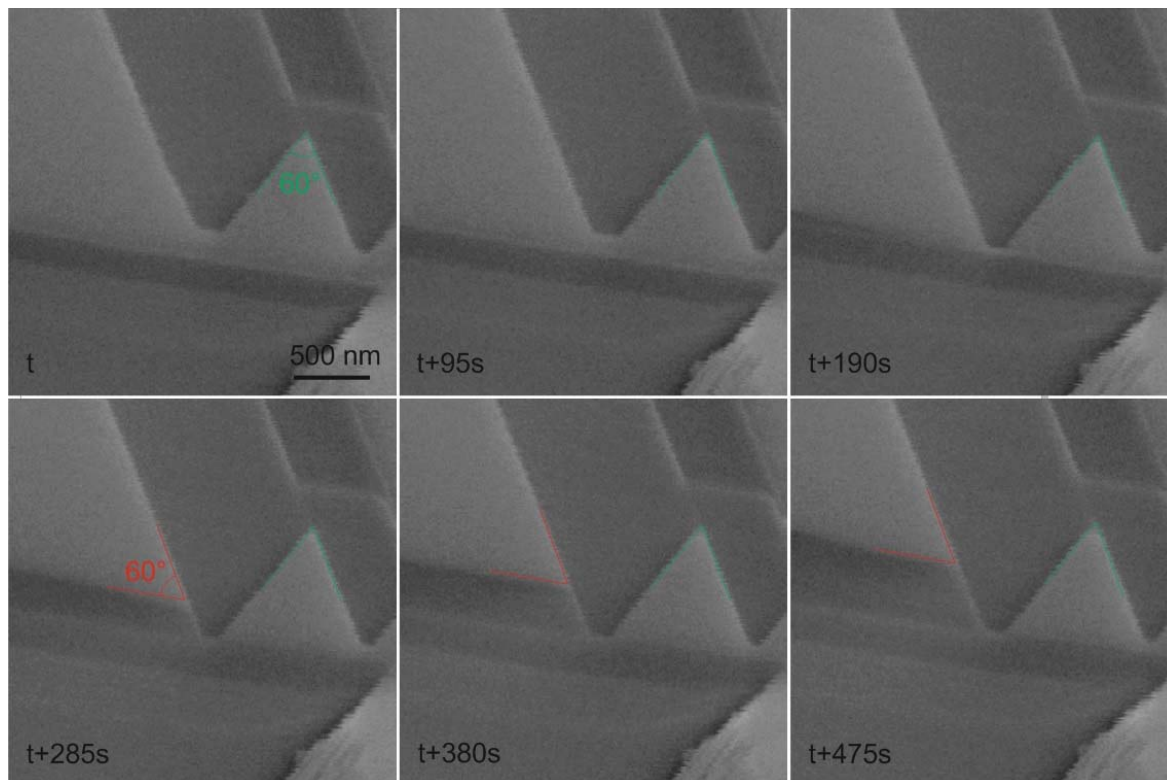

Figure 7. Sequence of *in situ* ESEM images recorded during the coalescence of aligned domains on Rh(111). The green and red lines highlight the intersection corner with angles of 60°. Conditions of growth: 900 °C on Rh(111) at a total pressure of 4.2×10^{-2} Pa (C_2H_4:H_2 = 1:10). Note that the angle of the concave corners remains the same during coalescence.

A series of STM images capturing the growth and coalescence of graphene on Rh(111) at 700 °C is presented in **Figure 8**. It is revealed that the kink creation at the growth front occurs in units of the Moiré lattice. Following the kink creation, C adatoms rapidly attach to this kink site and an entire row of Moiré pattern progresses along the edge.[42] Similarly to the *in situ* ESEM observations, the 60° angle of the concave corner remains unchanged during the coalescence process observed in the STM (**Figure 7**). Furthermore, a GB that follows the trajectory of the

concave corner is seen in the STM images (**Figure 8** and **Figure SI 5**), even though the 60° or 120° angle indicates alignment of the two graphene lattices. The domains on either side of the boundary are aligned to each other, but the respective Moiré-pattern and associated height corrugations at the edge do not coincide (**Figure 8e, f**). This observation shows that the seamless coalescence on substrates with a strong film–substrate interaction requires both: orientation alignment of the lattice and coincidence of the respective Moiré pattern.
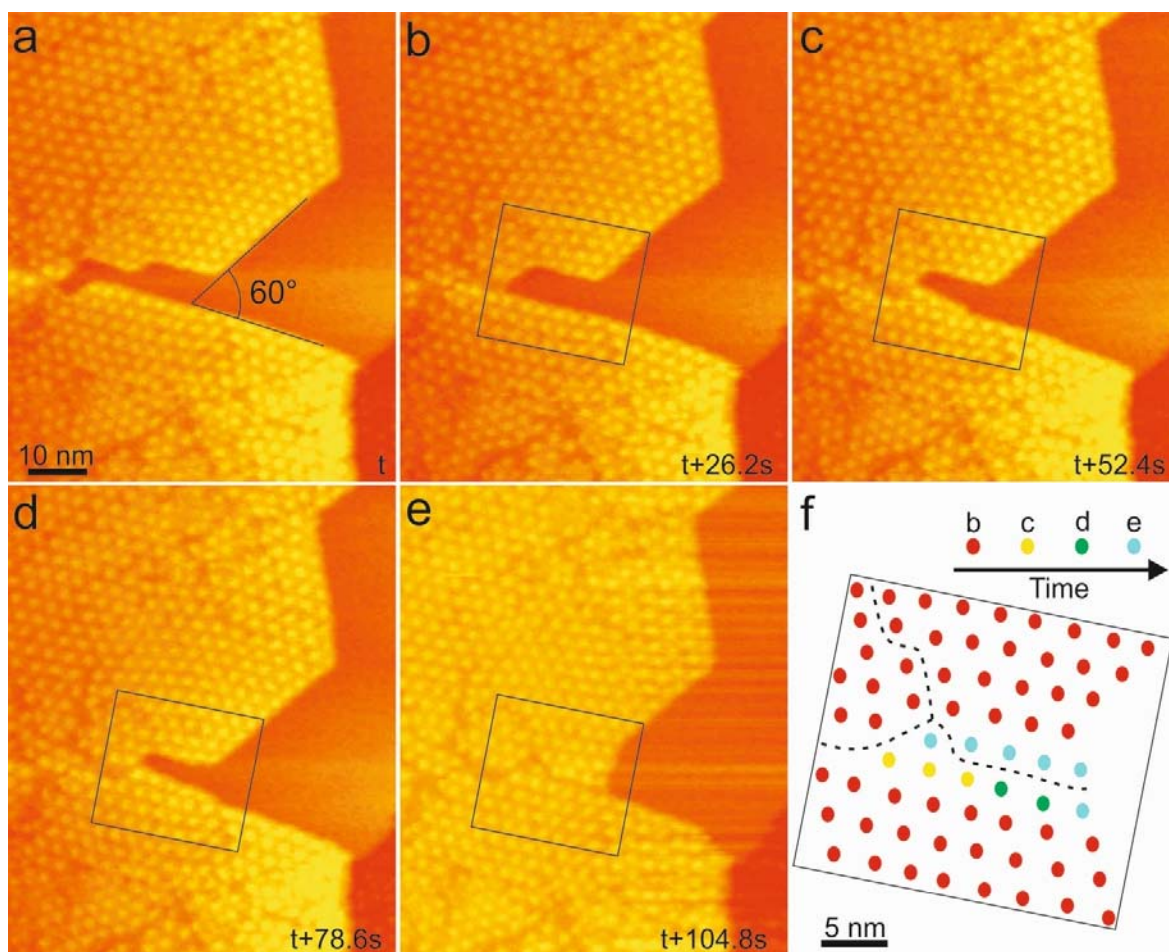

Figure 8. (a-e) *In situ* STM images recorded during graphene growth on Rh(111) at 700°C with a C_2H_4 pressure of 5.7×10^{-7} Pa. The STM images have been taken at a sample voltage of $V_b = -1.84$ V and a tunneling current of $I_t = 0.05$ nA. (f) Schematic representation of the time-dependent changes of the domain shown in (a-e). The superimposed colored dots correspond to protrusion areas (weak adsorption region) in Moiré supercell and were extracted from the black window present on frames (b-e). The dashed lines indicate the graphene GBs.

At higher pressure, multi-Moiré-kink (MMK) nucleation can occur at the growth front. This can be observed by *in situ* ESEM (**Figure 9** and **Supporting Movie 5**). The new kink that is created is coherent with the Moiré lattice of the grain. The 120° angle at the kink-site of a single crystalline grain can, in principle, be regarded as a representative for a concave corner between two co-oriented domains. The fact that formation of 19.1° edges is not observed at the 120° concave angle of a single crystal during the growth process is a consequence of the growth in Moiré units and thus, associated to a strong film-substrate interaction.
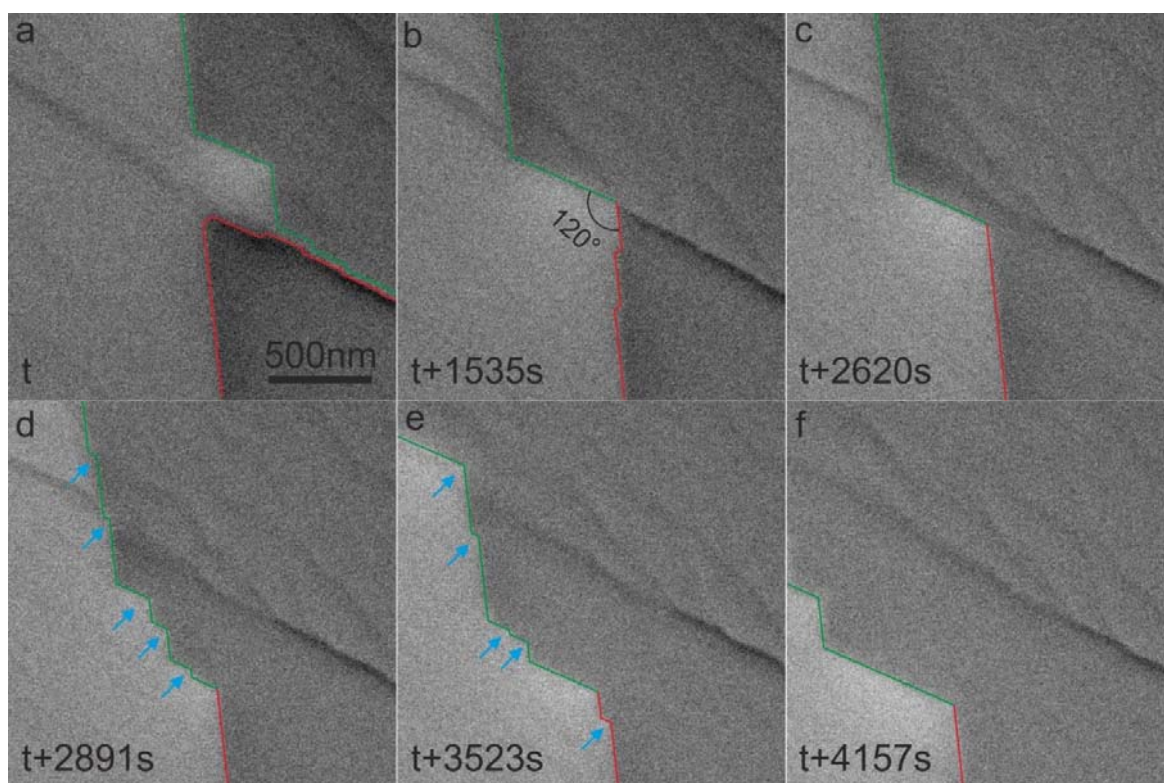

Figure 9. Time-lapse image series recorded during the coalescence of well-aligned domains on Rh(111) at 900°C and a total pressure of 25 Pa (C_2H_4:H_2 = 1:100). The green and red lines highlight the growth-fronts of the coalescing domains. The intersection corners remain at an angle of 120° throughout the coalescence process. Note that the angles of MMKs site, which are highlighted in (d, e) by blue arrows, are also 120°.

We also performed STM post-growth characterization of graphene films that were grown at 25 Pa in the ESEM. **Figure 10a** presents a stepped GB with steps in the height of a single Moiré supercell. A portion of it is shown at higher magnification in **Figure 10b**. A schematic view of the coalescence process between aligned domains is provided in **Figure 10c**. It shows how kink creation in units of Moiré cells can results in the formation of a GB with a stair-step shape in the case of non-coinciding Moiré lattices. The post-growth STM observation confirms that the modulated growth process in unit cells of the Moiré pattern, which was first observed by *in situ* STM at UHV conditions (**Figure 8**), also occurs during growth at relevant CVD conditions.
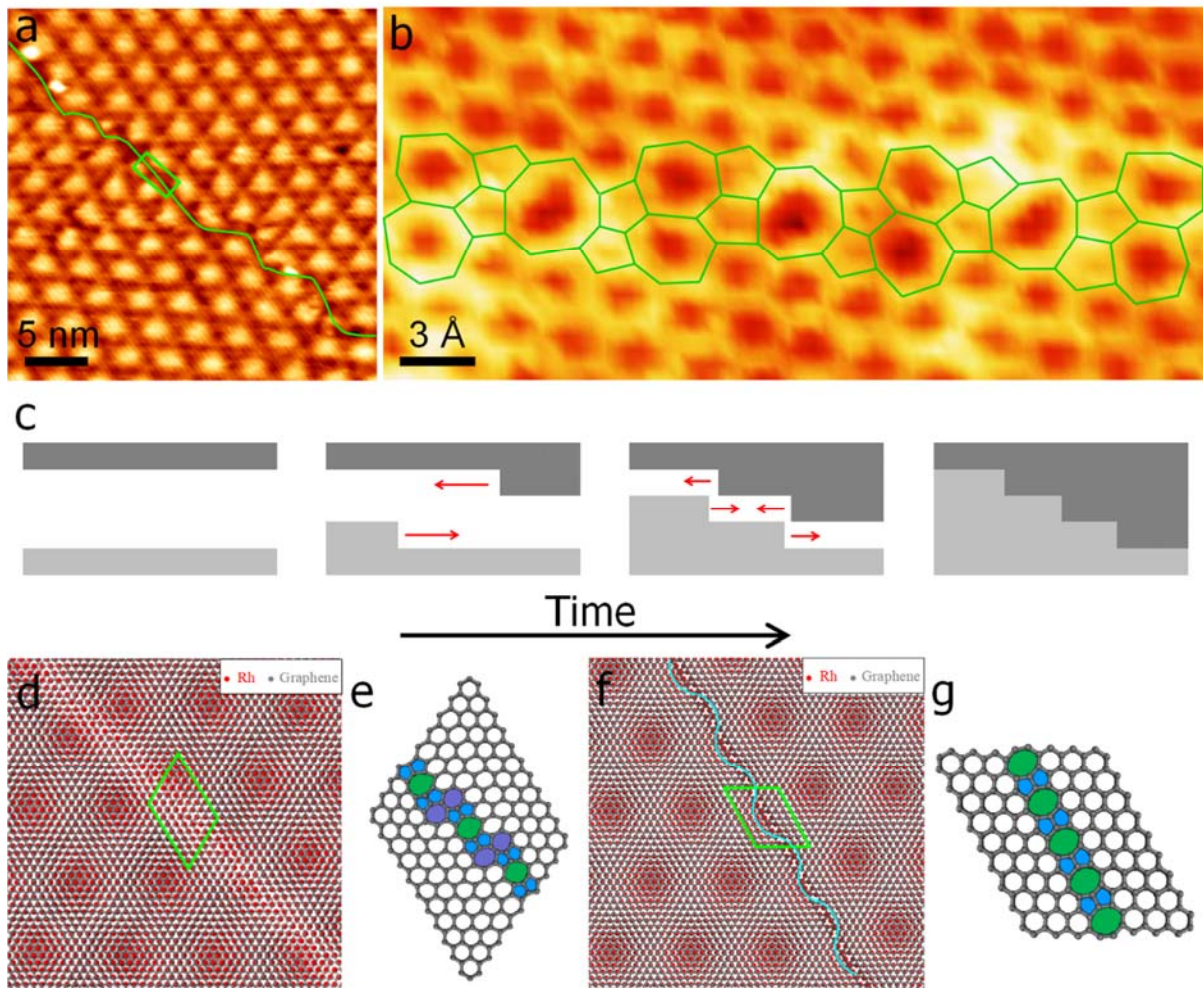
Figure 10. Post growth STM imaging reveals the GB structure on Rh(111). (a) STM overview image (28 nm × 28 nm) of the graphene GB (highlighted by a green line) observed on Rh(111) after CVD growth inside the ESEM chamber at a total pressure of 25 Pa ($C_2H_4:H_2$ = 1:100). (b) Atomically resolved graphene GB (magnification of the green square in (a)) together with a superimposed GB model. The GB model is realized through a linear chain of abutting pentagon pairs–octagon–pentagon pairs–heptagon pairs. (c) Schematic representation of the formation of a stair-stepped GB. Red arrows indicate the direction of kink growth. (d) and (f) Schematic representations of the relationship between the Moiré pattern of aligned domains and the resulting GB with two different stitching edges. The corresponding atomistic models of GB structures are depicted on (e) and (g). A sinusoidal curve (blue) is added in (g) as a guide to the eye, to facilitate the comparison of the Moiré period on both sides of the GB. Tunneling conditions: (a) V_s = 1 V, I_t = 0.3 nA; (b) V_s = 0.5 V, I_t = 0.5 nA.

In the following, we address the atomic structure of graphene GBs on the Rh substrate. In general, two types of GBs can stitch graphene domains together. In the case of rotated domains, the GB consists of a series of pentagon and heptagon carbon rings.[54] In the case of well-aligned domains, the GB structure consists of octagons that are separated by pairs of pentagons (55-8). Such a GB zipping of aligned domains has been documented for the case of graphene growth on Ni(111), for example.[64] As mentioned above, due to the strong interfacial interactions, the graphene domains are aligned on the Rh substrate. Therefore, the structure of graphene GBs on Rh should follow the GB zipping process and contain sections of pentagons and octagons (55-8). The high-resolution STM image in **Figure 10b** shows that the GB structure is composed of a linear chain of alternating pentagon pairs – octagon – pentagon pairs – heptagon pairs (55-8-55-77). The relationship between the graphene domains, with the 55-8-55-77 boundary structure, and the Moiré-pattern of graphene-Rh, $(12 \times 12)_C$ on $(11 \times 11)_{Rh}$, is sketched using a ball-and-stick representation in **Figure 10d,e**. Due to strong graphene–substrate interactions, the interfacial region at the grain boundary is highly strained and the Moiré pattern disrupted (**Figure 10a, d**). The formation of a linear chain of 55-8-55-77 rings allows a relaxation of the strain that results

from shear dislocations of the honeycomb network at the intersection of two shifted Moiré pattern.[64]

The 55-8-55-77 structure consists of a straight section of 55-8-55 units and an offset bridge of 77, which links two parallel 55-8-55 sections. This results in a zigzag GB, as shown in **Figure 10e**. Similar boundary structures have been observed in silica films grown on Ru.[65] Considering that the graphene is terminated by smooth zigzag edges during the growth in the attachment limited regime, we can deduce that the most prevalent feature of a GB connecting aligned domains with zigzag edges should be a straight chain of pentagon pairs with an octagon unit (55-8). As shown in **Figure 10f, g**, a 55-8 GB interfaces the two domains, featuring half of the Moiré spots on each side.[66] While the row of 55-8 units is the typical structure forming at straight GBs between aligned zigzag edges, the 55-8-55-77 GB forms at stepped GBs.

Generalization to other 2D materials and substrates

In the following, we generalize the findings obtained for graphene grown on Pt and Rh to other substrates and 2D materials.

We start with copper, which is presently the most popular substrate for graphene growth and shows a weak coupling strength with graphene. In the literature, there are several cases where the formation of rounded concave corners during the coalescence of aligned graphene domains is evident from provided images.[13, 67, 68] In some cases, it was either not noticed or commented, in others it was interpreted as a result of new nucleation events between adjacent domains at carbon defects.[69] In order to confirm that the rounding at concave corners is related to seamless coalescence, we repeated CVD growth of graphene on copper (see **Figure 11a**).

Switching from graphene to hexagonal-boron-nitride (*h*BN), which also shows a weak film-substrate interaction when grown on copper, we confirm that rounded concave corners are

observed during coalescence of aligned domains (see **Figure 11b**). Rounded concave corners with

19.1° edges also appear during the coalescence of transition metal dichalcogenides.[15, 70] As shown

in our previous work,[71] the frequent appearance of 19.1° edges can also be found during the

growth−etching−regrowth processes of monolayer GaSe domains. Thus, the appearance of 19.1°

edges and associated reduction of the angle at the concave corner seems to be general feature of

seamless coalescence of 2D materials on substrates that show a weak film–substrate interaction.

To provide an additional case, we performed CVD growth of MoS_2 on SiO_2.[72] The CVD growth

was performed in a S rich atmosphere.[73] Under such conditions, the triangular-shaped MoS_2

domains are terminated by S at zigzag edges.[74] As shown in **Figure 11c-d**, the formation of

rounded concave corners is observed during the coalescence of aligned MoS_2 domains. At higher

magnification, SEM imaging clearly reveals the ~19° tilted edges (highlighted by yellow arrows

in **Figure 11e**). The atomic structure of each MoS_2 edge is directly correlated with the mesoscopic

edge orientation,[45] and we thus can reproduce the detailed structure of the MoS_2 edges at the

rounded concave corner with 19.1° edges (see **Figure 11f**). The coalescence behavior of MoS_2

domains is thus very similar to the case of graphene islands that coalesce by seamless stitching.

To get a quantitative understanding of the coalescence process, we simulated the shape evolution

of monolayer MoS_2 domains during seamless coalescence using a phase field model (see **Figure

11g-k**).[75] The evolution of MoS_2 domains during growth were simulated, starting with two circular

nuclei (refer to **Supporting Note 4** for simulation details). The resulting polar plots of the

orientation dependent growth rates for the MoS_2 domains are shown in **Figure 11l**. The simulated

shape evolution of MoS_2 is in good agreement with the experimentally observed shapes and clearly

shows the formation of fast growing (19.1°) edges and fast filling of the concave corners. These

examples show that the relation between the appearance of a rounded concave corner and seamless coalescence can be generalized to other 2D materials that show 6-fold or 3-fold symmetry.

Overall, the appearance of rounded concave corners with 19.1° edges is just a macroscopic expression of the fact that attachment of new atoms and thus, kink creation, is energetically favorable at an unstrained concave corner. It is independent of the material type, as long as the film–substrate interaction is weak and can be used as a simple criterion for the judgement of seamless coalescence in weak film–substrate interactions.
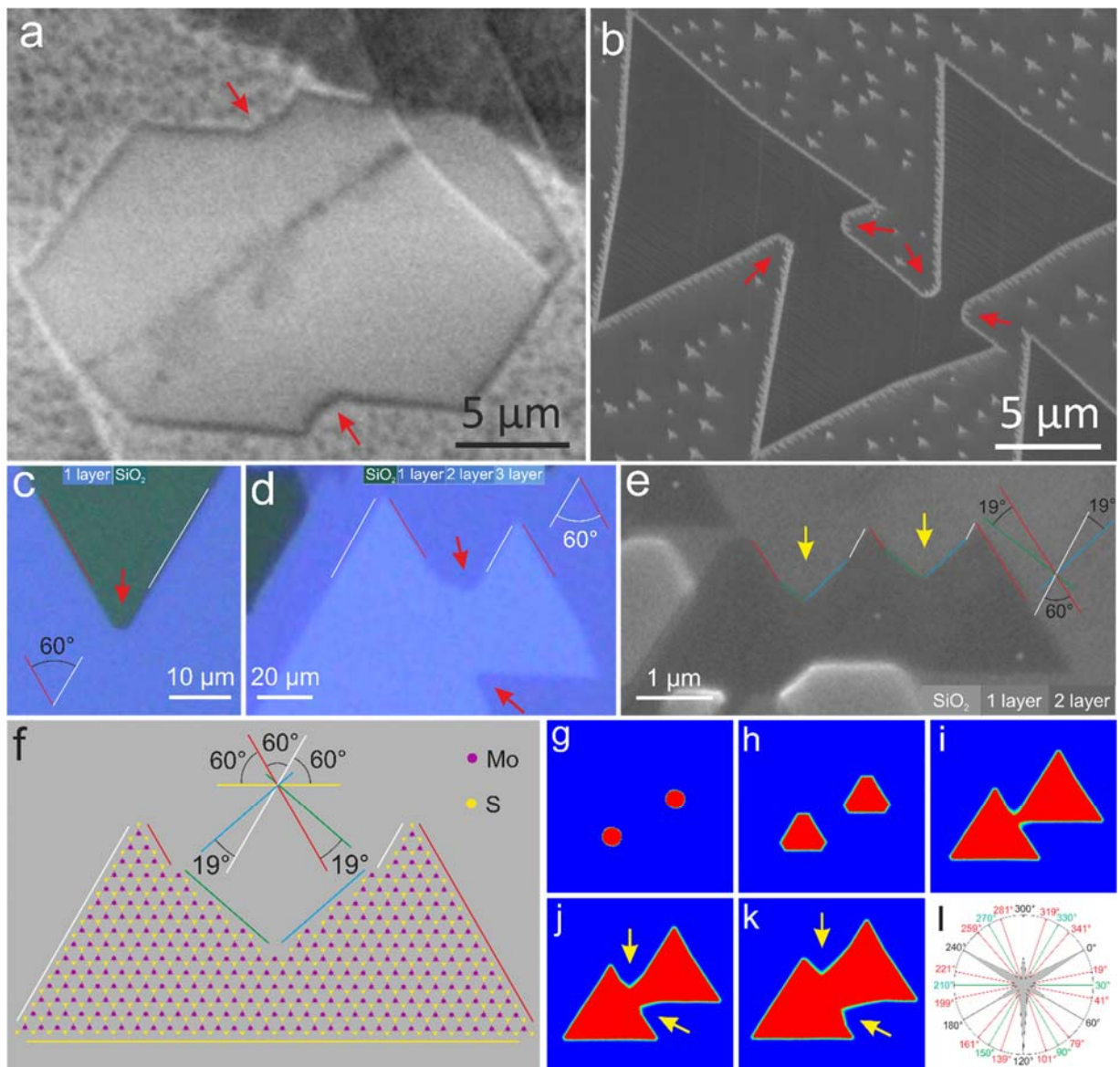
Figure 11. The shape of concave corners between coalescing domains in weak film–substrate interactions systems. (a) A scanning electron microscopy (SEM) image showing the coalescence of aligned graphene on Cu. (b) SEM image showing coalescence of aligned hBN on Cu. (c, d) Optical image of concave corner between aligned MoS_2 domains grown on SiO_2. The red arrows indicate rounded concave corners. (e) A SEM image showing the appearance of 19.1° edges at concave corners of aligned MoS_2 domains. (f) Schematic view showing the 19.1° edge and morphology evolution during coalescence. (g-k) Phase-field-theory simulation of the coalescence of aligned MoS_2 domains, and corresponding polar plots (l) showing the logarithm of relaxation time along different growth directions. A smaller relaxation time represents a lower growth barrier and thus a higher growth rate of an edge. Red color represents MoS_2, blue color represents the uncovered substrate. The yellow arrows indicate appearance of 19.1° edges at concave corners. In (c), (d) and (e), the number of layers can be abstracted by comparing the contrast in the images with the contrast legend in the respective panels.

In case of growth on substrates that show a strong film-substrate interaction, the lattice mismatch between film and substrate induces a buckling of the film. Modulation of the adsorption energy on the atomic scale leads to a growth in units of the Moiré cells. The seamless coalescence of two adjacent domains thus requires, in addition to the orientation alignment, also a coincidence of the respective Moiré pattern. Because of the growth modulation in Moiré units, the edges with highest kink-density (i.e, the 19.1° edges) do not form. Therefore, the angle of the concave corners remains unchanged during coalescence, even if the coalescence is seamless. A coalescence behavior similar to the case of graphene grown on Rh should be observed the case of other 2D materials that grow under the influence of a strong film–substrate interaction. Indeed, the MMKs forming at the growth front in hBN during growth on Ni (111) are indicative for a strong interaction. The observation that the angle between multi-Moiré-kink sites remains unchanged during growth, as shown in **Figure 12a-f**, is a further confirmation of a strong film-substrate interaction. Further *in situ* STM imaging of aligned hBN domains growing on Rh reveals cases of seamless and non-seamless coalescence under identical conditions (highlighted by green and purple arrows in **Figure 12g-k**, respectively). In both cases, the angle of the concave corner remains unchanged (see **Figure 12g-l**). Similar coalescence behaviors of hBN have been observed on Re,[76] Ni,[77] Co,[78] and on Ni-Cu

substrates,[79, 80] each characterized by strong interactions. Overall, we find that in the case of growth on strongly interacting substrates, there is no macroscopically observable growth feature that can be used to identify GB-free coalescence.
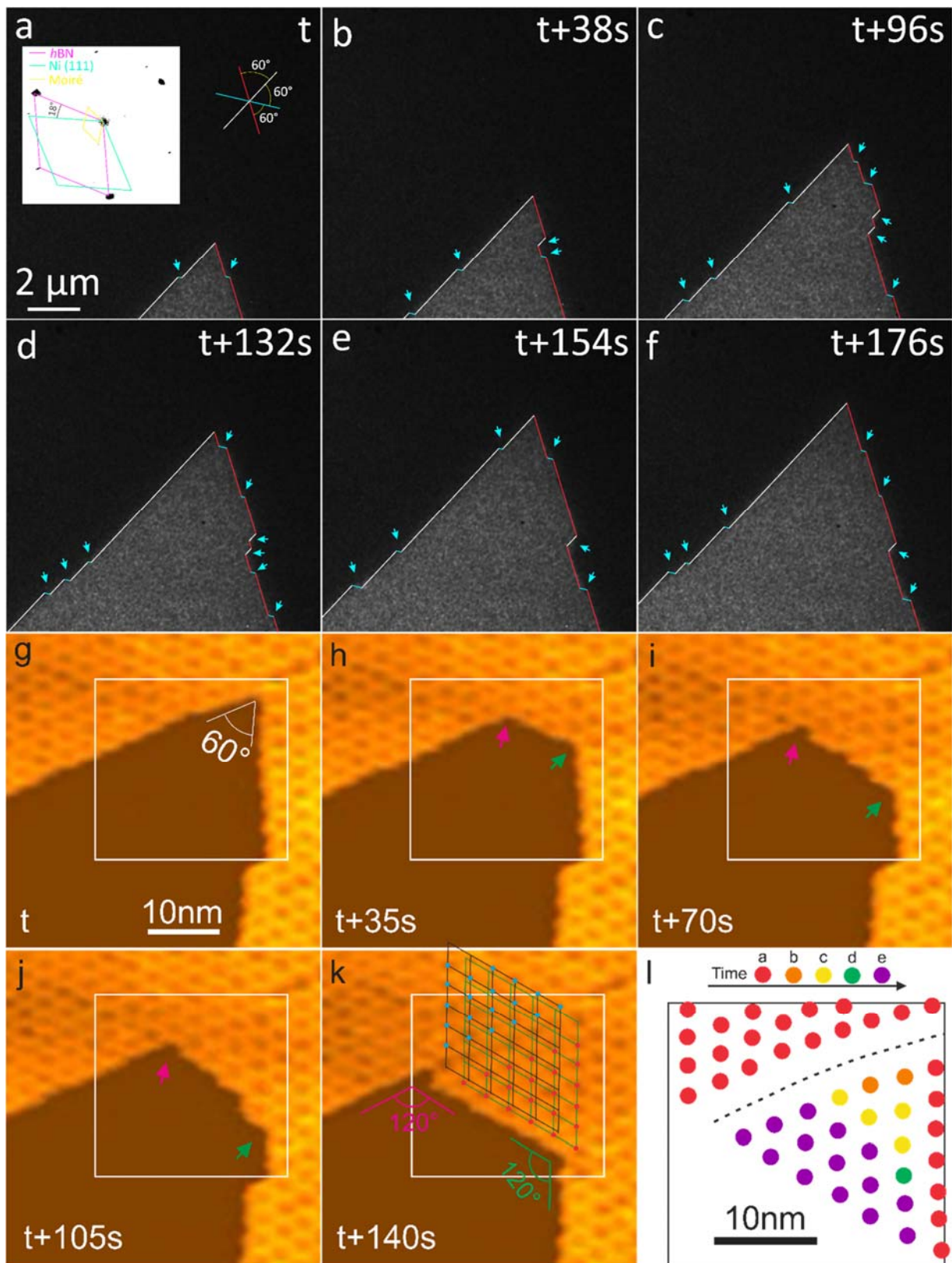
Figure 12. The shape of concave corners between merging domains growing under the influence of a strong film–substrate interaction. (a-f) Sequence of *in situ* PEEM images recorded during *h*BN growth on Ni(111) at 640 °C under a total pressure of 4.7×10^{-6} Pa (BH$_3$NH$_3$) showing MMKs creation on zigzag edges of *h*BN. The inset in (a) shows a low-energy electron diffraction (LEED) (50 eV) pattern recorded from the observed region. Rhombuses with different colors: purple, *h*BN; green, Ni(111); yellow, moiré superstructure. The different direction of zigzag edges is highlighted by different color. Note that the angles at MMKs sites, which are highlighted in (a-f) by blue arrows, measure 120° and remain unchanged during growing. The growth behavior of *h*BN on Ni is similar to the one of graphene on Rh (refer to Figure 9). (g-k) *In situ* STM images recorded during *h*BN growth on Rh(111) at 700 °C at a pressure of 1.2×10^{-7} Pa using borazine as precursor. The STM images were recorded at a sample voltage of $V_b = 1.0$ V and a tunneling current of $I_t = 0.05$ nA. The green and black grids in (k) indicate the lattice of the moiré pattern formed between *h*BN and the Rh(111). Note that red and blue dots in (k) highlight depression areas (strong adsorption region) in the Moiré supercell. The arrangement of the two lattices shows that the adjacent domains are aligned but incoherent in the respective Moiré corrugation. The purple arrows highlight the concave corner at which a GB is formed. The green arrows highlight a concave corner where coalescence is seamless. (l) Schematic representation of the time-dependent changes of the domain shown in (g-k). The superimposed colored dots correspond to depression areas in the Moiré supercell and were extracted from the area indicated by a white square in frames (g-k). The dashed line in (l) indicates the position of the GB. Note that the growth behavior of *h*BN is similar to graphene on Rh (the kink creation at the edge occurs in units of the Moiré lattice) and the angle of the concave corners remains the same during coalescence.

Conclusion

In summary, we studied the growth and coalescence behavior of 2D materials. Real-time multi-scale observation of 2D film growth dynamics at different length scales, from the atomic-to micrometer-scale, provides the missing clues for unravelling the influence of interfacial interaction strength on the coalescence processes. We demonstrate that atomistic processes can be traced in the dynamics that are observed at the micrometer-scale. Furthermore, it is shown that insights about factors that determine growth and coalescence under UHV conditions are valid for growth under relevant CVD conditions. Finally, by combining *in situ* experiments with theoretical calculations, it is shown that the experimental observations are in line with theoretical descriptions of mechanisms that determine 2D growth and coalescence.

In view of the similar growth mechanism of 2D materials, we propose that the coalescence mechanism derived in this work can guide the growth of crystalline 2D materials such as semiconducting transition metal dichalcogenides. We also suggest that macroscopic growth features, such as the rounded concave corners, can be used as convenient indicator for a judgement of the interaction strength between film and substrate. Most importantly, this work highlights the importance of correlative *in situ* experiments for a better understanding of 2D growth processes.

The broader significance of this work lies in the demonstration that a combination of complementary *in situ* methods can lead to a consistent picture of growth from the atomic to the millimeter scale and across the pressure-gap between surface-science UHV methods and industrially relevant CVD growth conditions.

Methods

In situ ESEM

In situ CVD growth experiments were performed inside the chamber of a modified commercial ESEM (*FEI Quantum 200*). The vacuum system of the ESEM was modified and upgraded with oil-free pre-vacuum pumps. The instrument is equipped with a home-made laser heating stage, a gas supply unit (mass flow controllers from *Bronkhorst*) and a mass spectrometer (*Pfeiffer OmniStar*) for the analysis of the chamber atmosphere. Owing to the use of rubber O-rings for the sealing and the fact that the chamber cannot be baked out, the base pressure of the instrument is around 2×10^{-5} Pa, with a residual gas composition mostly comprising water, N_2 and O_2.[34] After each sample loading, the chamber was pumped out to around 10^{-3} Pa, purged with pure nitrogen and pumped again to 10^{-3} Pa successively for several times. Under CVD growth conditions, the pressure is six orders of magnitude higher than the base pressure and constitutes mostly H_2

(99.9995% purity) and C_2H_4 (99.95% purity). Samples of sizes ranging from 4×4 to 5×5 mm are extracted from a 0.5 mm-thick single crystalline Pt and Rh (99.999% purity). Prior to all CVD growth experiments, the chamber of the ESEM was plasma cleaned. The crystals were annealed at 1000 °C under a hydrogen flow of 10 sccm at 25 Pa for more than 48 h inside the chamber. The temperature was measured *via* a B-type thermocouple that was spot-welded onto the substrate, which simultaneously served to ground the sample. CVD growth was performed at temperatures ranging from 700°C to 1000°C, with a pressure in the chamber ranging from 10^{-3} Pa to 25 Pa. Hydrogen etching was performed under 10 sccm H_2 at 900 °C at 25 Pa. During the experiments, the microscope was operated at an acceleration voltage of 5.0–7.5 kV. Images were recorded by an Everhart Thornley detector (ETD) / a large field detector (LFD) during CVD growth and etching under high-vacuum and low-vacuum conditions, respectively. No influence of the electron beam on the growth and etching process could be observed. The imaged regions and their respective surroundings showed similar behavior, as evidenced by changing the magnification or by moving the sample under the beam. Furthermore, no electron beam induced contamination was observed at elevated temperatures.

In situ LEEM/LEED

Graphene growth under UHV were conducted in a SPECS low-energy electron microscopy (LEEM) system which connected to the Vacuum Interconnected Nanotech Workstation (NANO-X) of Suzhou Institute of Nano-Tech and Nano-Bionics, the Chinese Academy of Sciences, which is installed with a preparation chamber and a main chamber. Imaging for graphene domains growth on Rh/Pt(111), incident electron beam energies are chosen by 7 eV. In this system, LEED can also be performed to investigate surface structure after graphene growth. The incident electron beam energies are always kept at 50 eV during μ-LEED measurements.

In situ STM

In situ STM observations were performed on Rh(111) under low vacuum conditions within a STM that can be operated under pressures ranging from UHV up to 10^{-5} Pa and at elevated.[42] Temperatures were measured using a K-type thermocouple that was spot-welded directly onto the sample. Gas pressures were measured by an ionization gauge that was calibrated for C_2H_4. The clean Rh(111) surface was exposed to 1.3×10^{-8} Pa of ethylene at room temperature. During heating to 700°C, the pressure of ethylene was increased from 1.3×10^{-8} to 1.5×10^{-6} Pa in order to maintain growth irrespective of the increasing coverage of the active catalytic surface area. The temperature was held at 700°C throughout the whole *in situ* STM observation of graphene growth. In this work, we show STM movies that were recorded in the phase where the pressure was 5.7×10^{-7} Pa.

Ex situ STM

STM measurements were performed at room temperature in an UHV system with base pressure in the range of 10^{-8} Pa, equipped with STM, LEED apparatus, Ar^+ sputtering gun, laser heating stage, and gas feeding system. The images were recorded with a constant current mode using a home-made W-tip.

In situ NAP-XPS

The *in situ* NAP-XPS experiments were performed at the ISSIS beamline of the FHI located at the BESSY II synchrotron facility in Berlin. The high pressure setup consists mainly of a reaction cell attached to a set of differentially pumped electrostatic lenses and a differential- pumped analyzer (*Phoibos 150 Plus, SPECS GmbH*), as described elsewhere.[81] The spectra were collected in normal emission with a probe size of $\approx$ 150µm×80µm.

Gases (H_2, C_2H_4) were introduced to the reaction cell using calibrated mass flow controllers (*Bronkhorst*). Prior to gas exposure the samples were heated up to 900°C from the back using an external IR-laser (cw, 808 nm). The temperature was controlled *via* a K-type thermocouple in direct contact with the sample surface.

Sample contamination was checked by survey spectra at the beginning of each experiment. The photo electron spectra were taken at photon energies of 490 eV (Rh_{3d}), 240 eV (Pt_{4f}), 425 eV (C_{1s}) and 680 eV (O_{1s}), respectively, with a spectral resolution of 0.3 eV. The kinetic energies of the electrons correspond to an electron mean free path of $\approx$ 7 Å. The total XPS information depth λ is $\approx$ 2 nm, that is, 95% of all detected electrons originate from 3λ.[82] For XPS analysis, the photoelectron binding energy (BE) is referenced to the Fermi edge, and the spectra are normalized to the incident photon flux. Background correction was performed using a Shirley background.[83] The spectra were fitted following the Levenberg-Marquardt algorithm to minimize the χ^2. Peak shapes were modeled by using asymmetric Doniach-Sunjic functions convoluted with Gaussian profiles.[84] The accuracy of the fitted peak positions is $\approx$ 0.05 eV.

DFT calculations

All DFT calculations are performed by using the Vienna *ab initio* simulation Package (VASP).[85] Local density approximation (LDA) is used for the exchange correlation functional.[86] The electron-ion interaction is treated by the projected augmented wave (PAW) method.[86] An energy cutoff of 400 eV is used for the plan wave basis. To calculate the growth behaviors of graphene coalescence in presence of two neighboring graphene domains with a misorientation angle, a graphene flake with a concave structure and a GB, with a misorientation angle of 21.8°, is constructed. The graphene flake is modelled in an orthorhombic unit cell that is large enough to avoid interactions between repetitive images. Its growth process is shown in **Figure SI 6a**. C atoms

are attached to the concave structure consecutively. A GB-free graphene flake, with a concave corner of 120°, is also constructed to study the growth of coalesced graphene domains that are well-aligned (**Figure SI 6b**). All these structures are fully optimized until the force on each atom is less than 0.01 eV/Å by the conjugate gradient method. Only Gama point is used for the Monkhorst–Pack k-point sampling.

The formation energy change, ΔE_F, during the growth of concave structures formed by coalescence of neighboring graphene domains is defined by

$$\Delta E_F = E_i - E_{\mathrm{Re}f} - N_C \times \varepsilon_C - N_H \times \mu_H$$

where E_i is the energy of the structure at the ith growth step, E_{Ref} is the energy of the initial structure for growth calculation, N_C and N_H are the number of C and H atoms attached to the initial structure, ε_C is the energy of a C atom in a perfect monolayer graphene, μ_H is the chemical potential of H atoms. μ_H is determined by setting the ΔE_F of the final growth structure in **Figure SI 6a** to be 0, because this structure recovers to the concave structure of the initial growth configuration.

Author Contributions

Z.-J.W. and M.-G.W. modified the ESEM, planned and conducted the *in situ* growth and etching experiments and wrote the manuscript. Z.-J.W did most of the ESEM and STM data analysis; theoretical simulations and implementation of the obtained results was done by J.D. and F.D.; *ex situ* STM measurements were performed by L.L., Y.C., Q.F., Q.L. and Z.-J.W.; G.D. and J.W.M.F conducted the *in situ* STM measurements; R.B. and Z.-J.W. conducted the *in situ* NAP-XPS measurement; Y.Y., W.W., and B.X. conducted the *in situ* PEEM measurement. Important contributions to the interpretation of the results, conception and writing of the manuscript were

made by Z.-J.W., F.D., and M.-G.W. All the authors discussed the results and commented on the manuscript.

Associated Content

Notes

The authors declare no competing financial interest.

Supporting Information Available:

Detailed simulation for kinetic Wulff construction of coalescence process; DFT calculations of graphene coalescence; Simulation of MoS_2 coalescence process with the phase field model; Structures used for the calculation of growth of coalesced graphene domains; ESEM movies

showing the metal-catalyzed CVD growth and coalescence of graphene on the Pt/Rh surface at
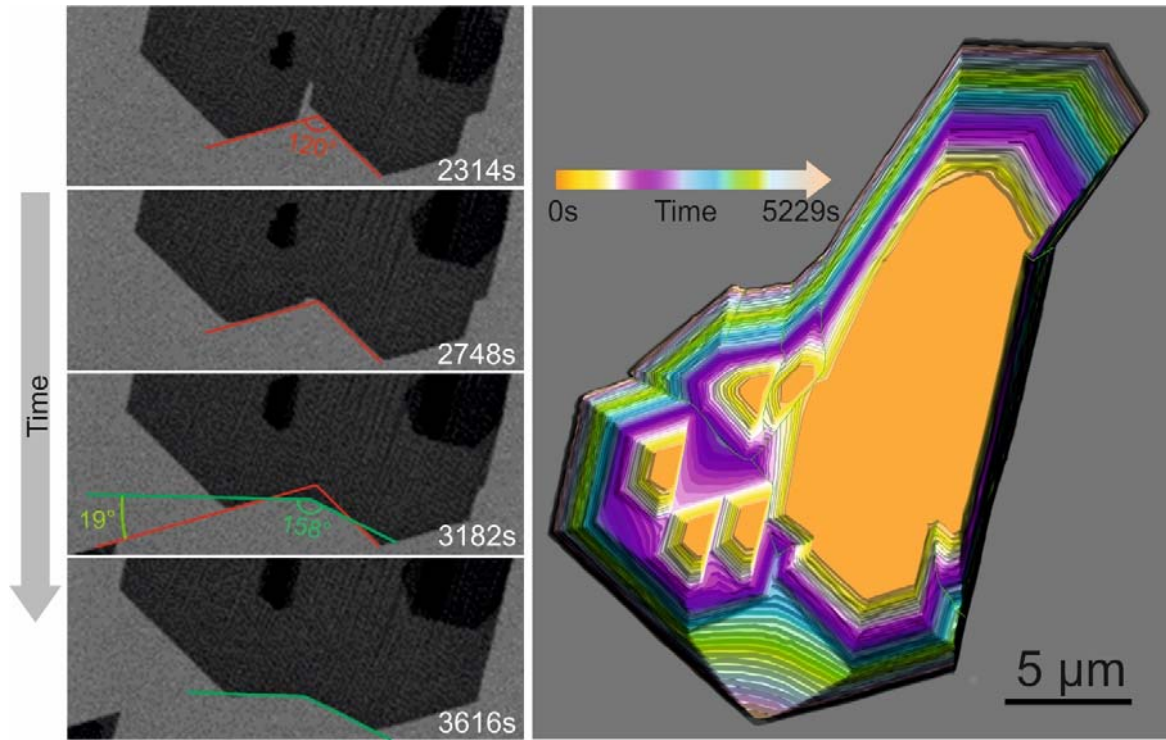
900°C.

REFERENCES

1.   Geim, A. K.; Novoselov, K. S. The Rise of Graphene. *Nat. Mater.* **2007**, *6*, 183-191.
2.   Novoselov, K. S.; Fal'ko, V. I.; Colombo, L.; Gellert, P. R.; Schwab, M. G.; Kim, K. A Roadmap for Graphene. *Nature* **2012**, *490*, 192-200.
3.   Xiao, X. Y.; Li, Y. C.; Liu, Z. P. Graphene Commercialization. *Nat. Mater.* **2016**, *15*, 697-698.
4.   Hao, Y. F.; *et al*. The Role of Surface Oxygen in the Growth of Large Single-Crystal Graphene on Copper. *Science* **2013**, *342*, 720-723.
5.   Gao, L. B.; *et al*. Repeated Growth and Bubbling Transfer of Graphene with Millimetre-Size Single-Crystal Grains Using Platinum. *Nat. Commun.* **2012**, *3*, 699.
6.   Chen, S. S.; *et al*. Millimeter-Size Single-Crystal Graphene by Suppressing Evaporative Loss of Cu During Low Pressure Chemical Vapor Deposition. *Adv. Mater.* **2013**, *25*, 2062-2065.
7.   Sutter, P. W.; Flege, J. I.; Sutter, E. A. Epitaxial Graphene on Ruthenium. *Nat. Mater.* **2008**, *7*, 406-411.
8.   Pan, Y.; Zhang, H. G.; Shi, D. X.; Sun, J. T.; Du, S. X.; Liu, F.; Gao, H. J. Highly Ordered, Millimeter-Scale, Continuous, Single-Crystalline Graphene Monolayer Formed on Ru (0001). *Adv. Mater.* **2009**, *21*, 2777-2780.
9.   Iwasaki, T.; Park, H. J.; Konuma, M.; Lee, D. S.; Smet, J. H.; Starke, U. Long-Range Ordered Single-Crystal Graphene on High-Quality Heteroepitaxial Ni Thin Films Grown on MgO(111). *Nano Lett.* **2011**, *11*, 79-84.
10.   Wang, Q. H.; Kalantar-Zadeh, K.; Kis, A.; Coleman, J. N.; Strano, M. S. Electronics and Optoelectronics of Two-Dimensional Transition Metal Dichalcogenides. *Nature Nanotechnology* **2012**, *7*, 699-712.
11.   Liu, K. K.; *et al*. Growth of Large-Area and Highly Crystalline MoS2 Thin Layers on Insulating Substrates. *Nano Letters* **2012,** *12*, 1538-1544.
12.   Lee, Y. H.; *et al*. Synthesis of Large-Area MoS$_2$ Atomic Layers with Chemical Vapor Deposition. *Adv. Mater.* **2012**, *24*, 2320-2325.
13.   Van Luan, N.; *et al*. Seamless Stitching of Graphene Domains on Polished Copper (111) Foil. *Adv. Mater.* **2015**, *27*, 1376-1382.
14.   Xu, X. Z.; *et al*. Ultrafast Epitaxial Growth of Metre-Sized Single-Crystal Graphene on Industrial Cu Foil. *Sci. Bull.* **2017**, *62*, 1074-1080.
15.   Lee, J. S.; *et al*. Wafer-Scale Single-Crystal Hexagonal Boron Nitride Film *via* Self-Collimated Grain Formation. *Science* **2018**, *362*, 817-821.
16.   Lin, L.; Deng, B.; Sun, J. Y.; Peng, H. L.; Liu, Z. F. Bridging the Gap between Reality and Ideal in Chemical Vapor Deposition Growth of Graphene. *Chem. Rev.* **2018**, *118*, 9281-9343.

17.   Loginova, E.; Bartelt, N. C.; Feibelman, P. J.; McCarty, K. F. Evidence for Graphene Growth by C Cluster Attachment. *New J. Phys.* **2008**, *10*, 093026.
18.   Wofford, J. M.; Nie, S.; McCarty, K. F.; Bartelt, N. C.; Dubon, O. D. Graphene Islands on Cu Foils: The Interplay between Shape, Orientation, and Defects. *Nano Lett.* **2010**, *10*, 4890-4896.
19.   Terasawa, T. O.; Saiki, K. Radiation-Mode Optical Microscopy on the Growth of Graphene. *Nat. Commun.* **2015**, *6*, 6834.
20.   Sutter, P.; Cortes, R.; Lahiri, J.; Sutter, E. Interface Formation in Monolayer Graphene-Boron Nitride Heterostructures. *Nano Lett.* **2012**, *12*, 4869-4874.
21.   Sutter, P.; Huang, Y.; Sutter, E. Nanoscale Integration of Two-Dimensional Materials by Lateral Heteroepitaxy. *Nano Lett.* **2014**, *14*, 4846-4851.
22.   Cui, Y.; Fu, Q.; Zhang, H.; Tan, D. L.; Bao, X. H. Dynamic Characterization of Graphene Growth and Etching by Oxygen on Ru(0001) by Photoemission Electron Microscopy. *J. Phys. Chem. C* **2009**, *113*, 20365-20370.
23.   Dong, G. C.; van Baarle, D. W.; Rost, M. J.; Frenken, J. W. M. Graphene Formation on Metal Surfaces Investigated by *in situ* Scanning Tunneling Microscopy. *New J. Phys.* **2012**, *14*, 053033.
24.   Patera, L. L.; Bianchini, F.; Africh, C.; Dri, C.; Soldano, G.; Mariscal, M. M.; Peressi, M.; Comelli, G. Real-Time Imaging of Adatom-Promoted Graphene Growth on Nickel. *Science* **2018**, *359*, 1243-1246.
25.   Gao, L. B.; Ren, W. C.; Zhao, J. P.; Ma, L. P.; Chen, Z. P.; Cheng, H. M. Efficient Growth of High-Quality Graphene Films on Cu Foils by Ambient Pressure Chemical Vapor Deposition. *Appl. Phys. Lett.* **2010**, *97*, 183109.
26.   Vlassiouk, I.; Fulvio, P.; Meyer, H.; Lavrik, N.; Dai, S.; Datskos, P.; Smirnov, S. Large Scale Atmospheric Pressure Chemical Vapor Deposition of Graphene. *Carbon* **2013**, *54*, 58-67.
27.   Freund, H. J.; Kuhlenbeck, H.; Libuda, J.; Rupprechter, G.; Baumer, M.; Hamann, H. Bridging the Pressure and Materials Gaps between Catalysis and Surface Science: Clean and Modified Oxide Surfaces. *Top. Catal.* **2001**, *15*, 201-209.
28.   Meca, E.; Lowengrub, J.; Kim, H.; Mattevi, C.; Shenoy, V. B. Epitaxial Graphene Growth and Shape Dynamics on Copper: Phase-Field Modeling and Experiments. *Nano Lett.* **2013**, *13*, 5692-5697.
29.   Jacobberger, R. M.; Arnold, M. S. Graphene Growth Dynamics on Epitaxial Copper Thin Films. *Chem. Mater.* **2013,** *25*, 871-877.
30.   Artyukhov, V. I.; Hao, Y.; Ruoff, R. S.; Yakobson, B. I. Breaking of Symmetry in Graphene Growth on Metal Substrates. *Phys. Rev. Lett.* **2015**, *114*, 115502.
31.   Preobrajenski, A. B.; Ng, M. L.; Vinogradov, A. S. Mårtensson, N. Controlling Graphene Corrugation on Lattice-Mismatched Substrates. *Phys. Rev. B* **2008**, *78*, 073401.
32.   Batzill, M. The Surface Science of Graphene: Metal Interfaces, CVD Synthesis, Nanoribbons, Chemical Modifications, and Defects. *Surf. Sci. Rep.* **2012**, *67*, 83-115.
33.   Wang, Z. J.; *et al*. Direct Observation of Graphene Growth and Associated Copper Substrate Dynamics by in Situ Scanning Electron Microscopy. *ACS Nano* **2015**, *9*, 1506-1519.
34.   Wang, Z. J.; Dong, J. C.; Cui, Y.; Eres, G.; Timpe, O.; Fu, Q.; Ding, F.; Schloegl, R.; Willinger, M. G. Stacking Sequence and Interlayer Coupling in Few-Layer Graphene Revealed by *in situ* Imaging. *Nature Communications* **2016**, *7*, 13256.

35.   Blume, R.; *et al.* The Influence of Intercalated Oxygen on the Properties of Graphene on Polycrystalline Cu under Various Environmental Conditions. *Phys. Chem. Chem. Phys.* **2014**, *16*, 25989-26003.

36.   Kidambi, P. R.; Bayer, B. C.; Blume, R.; Wang, Z.-J.; Baehtz, C.; Weatherup, R. S.; Willinger, M.-G.; Schloegl, R.; Hofmann, S. Observing Graphene Grow: Catalyst-Graphene Interactions during Scalable Graphene Growth on Polycrystalline Copper. *Nano Lett.* **2013,** *13*, 4769-4778.

37.   Sutter, P.; Sadowski, J. T.; Sutter, E. Graphene on Pt(111): Growth and Substrate Interaction. *Phys. Rev. B* **2009**, *80*, 245411.

38.   Coraux, J.; *et al.* Growth of Graphene on Ir(111). *New J. Phys.* **2009**, *11*, 023006.

39.   Vlassiouk, I.; Regmi, M.; Fulvio, P. F.; Dai, S.; Datskos, P.; Eres, G.; Smirnov, S. Role of Hydrogen in Chemical Vapor Deposition Growth of Large Single-Crystal Graphene. *ACS Nano* **2011**, *5*, 6069-6076.

40.   Wang, B.; Caffio, M.; Bromley, C.; Fruchtl, H.; Schaub, R. Coupling Epitaxy, Chemical Bonding, and Work Function at the Local Scale in Transition Metal-Supported Graphene. *ACS Nano* **2010**, *4*, 5773-5782.

41.   Voloshina, E. N.; Dedkov, Y. S.; Torbrugge, S.; Thissen, A.; Fonin, M. Graphene on Rh(111): Scanning Tunneling and Atomic Force Microscopies Studies. *Appl. Phys. Lett.* **2012**, *100*, 241606.

42.   Dong, G. C.; Frenken, J. W. M. Kinetics of Graphene Formation on Rh(111) Investigated by *In Situ* Scanning Tunneling Microscopy. *ACS Nano* **2013**, *7*, 7028-7033.

43.   Gotterbarm, K.; Zhao, W.; Hofert, O.; Gleichweit, C.; Papp, C.; Steinruck, H. P. Growth and Oxidation of Graphene on Rh(111). *Phys. Chem. Chem. Phys.* **2013**, *15*, 19625-19631.

44.   Merino, P.; Svec, M.; Pinardi, A. L.; Otero, G.; Martin-Gago, J. A. Strain-Driven Moire Superstructures of Epitaxial Graphene on Transition Metal Surfaces. *ACS Nano* **2011**, *5*, 5627-5634.

45.   Dong, J.; Zhang, L.; Ding, F. Kinetics of Graphene and 2D Materials Growth. *Adv. Mater.* **2019**, *31*, 1801583.

46.   Gao, M.; Pan, Y.; Huang, L.; Hu, H.; Zhang, L. Z.; Guo, H. M.; Du, S. X.; Gao, H. J. Epitaxial Growth and Structural Property of Graphene on Pt(111). *Appl. Phys. Lett.* **2011**, *98*, 033101.

47.   Zhang, Y.; Li, Z.; Kim, P.; Zhang, L. Y.; Zhou, C. W. Anisotropic Hydrogen Etching of Chemical Vapor Deposited Graphene. *ACS Nano* **2012**, *6*, 126-132.

48.   Yakobson, B. I.; Ding, F. Observational Geology of Graphene, at the Nanoscale. *ACS Nano* **2011**, *5*, 1569-1574.

49.   Geng, D. C.; Wu, B.; Guo, Y. L.; Luo, B. R.; Xue, Y. Z.; Chen, J. Y.; Yu, G.; Liu, Y. Q. Fractal Etching of Graphene. *J. Am. Chem. Soc.* **2013**, *135*, 6431-6434.

50.   Ma, T.; Ren, W. C.; Zhang, X. Y.; Liu, Z. B.; Gao, Y.; Yin, L. C.; Ma, X. L.; Ding, F.; Cheng, H. M. Edge-Controlled Growth and Kinetics of Single-Crystal Graphene Domains by Chemical Vapor Deposition. *Proc. Natl. Acad. Sci. U. S. A.* **2013**, *110*, 20386-20391.

51.   Guo, W.; *et al.* Governing Rule for Dynamic Formation of Grain Boundaries in Grown Graphene. *ACS Nano* **2015**, *9*, 5792-5798.

52.   Kim, K.; *et al.* Selective Metal Deposition at Graphene Line Defects by Atomic Layer Deposition. *Nat. Commun.* **2014**, *5*, 4781.

53.   Yu, S. U.; Park, B.; Cho, Y.; Hyun, S.; Kim, J. K.; Kim, K. S. Simultaneous Visualization of Graphene Grain Boundaries and Wrinkles with Structural Information by Gold Deposition. *ACS Nano* **2014**, *8*, 8662-8668.

54.   Huang, P. Y.; *et al*. Grains and Grain Boundaries in Single-Layer Graphene Atomic Patchwork Quilts. *Nature* **2011**, *469*, 389-392.

55.   Ma, T.; *et al*. Tailoring the Thermal and Electrical Transport Properties of Graphene Films by Grain Size Engineering. *Nat. Commun.* **2017**, *8*, 14486.

56.   Duong, D. L.; *et al*. Probing Graphene Grain Boundaries with Optical Microscopy. *Nature* **2012**, *490*, 235-239.

57.   Sekerka, R. F. Equilibrium and Growth Shapes of Crystals: How Do They Differ and Why Should We Care? *Crystal Research and Technology* **2005**, *40*, 291-306.

58.   Wang, D. M.; *et al*. Thermally Induced Graphene Rotation on Hexagonal Boron Nitride. *Phys. Rev. Lett.* **2016**, *116*,126101.

59.   Rogge, P. C.; Thuermer, K.; Foster, M. E.; McCarty, K. F.; Dubon, O. D.; Bartelt, N. C. Real-Time Observation of Epitaxial Graphene Domain Reorientation. *Nat. Commun.* **2015**, *6*, 6880.

60.   Yu, Q. K.; *et al*. Control and Characterization of Individual Grains and Grain Boundaries in Graphene Grown by Chemical Vapour Deposition. *Nat. Mater.* **2011,** *10*, 443-449.

61.   Babenko, V.; *et al*. Rapid Epitaxy-Free Graphene Synthesis on Silicidated Polycrystalline Platinum. *Nat. Commun.* **2015**, *6*, 7536.

62.   Hu, J. X.; *et al*. Roles of Oxygen and Hydrogen in Crystal Orientation Transition of Copper Foils for High-Quality Graphene Growth. *Sci. Rep.* **2017**, *7*, 45358.

63.   Zhu, S. Y.; Li, Q. F.; Chen, Q.; Liu, W. H.; Li, X.; Zhang, J.; Wang, Q. K.; Wang, X. L.; Liu, H. Z. Cu Hill and Graphene Grain Evolution in the Synthesis of Millimeter-Sized Single Crystal Graphene during Low Pressure Chemical Vapor Deposition. *Rsc Advances* **2014**, *4*, 32941-32945.

64.   Lahiri, J.; Lin, Y.; Bozkurt, P.; Oleynik, II; Batzill, M., An extended defect in graphene as a metallic wire. *Nat. Nanotechnol.* **2010,** *5* (5), 326-329.

65.   Burson, K. M.; Buchner, C.; Heyde, M.; Freund, H. J. Assessing the Amorphousness and Periodicity of Common Domain Boundaries in Silica Bilayers on Ru(0001). *J. Phys. Condens. Matter* **2017**, *29*, 035002.

66.   Pochet, P.; McGuigan, B. C.; Coraux, J.; Johnson, H. T. Toward Moire Engineering in 2D Materials *via* Dislocation Theory. *Appl. Mater. Today* **2017**, *9*, 240-250.

67.   Shi, Y. G.; Wang, D.; Zhang, J. C.; Zhang, P.; Shi, X. F.; Hao, Y. Fabrication of Single-Crystal Few-Layer Graphene Domains on Copper by Modified Low-Pressure Chemical Vapor Deposition. *Crystengcomm* **2014**, *16*, 7558-7563.

68.   van Gastel, R.; *et al*. Selecting a Single Orientation for Millimeter Sized Graphene Sheets. *Appl. Phys. Lett.* **2009**, *95*, 121901.

69.   Fan, L. L.; Li, Z.; Li, X.; Wang, K. L.; Zhong, M. L.; Wei, J. Q.; Wu, D. H.; Zhu, H. W. Controllable Growth of Shaped Graphene Domains by Atmospheric Pressure Chemical Vapour Deposition. *Nanoscale* **2011**, *3*, 4946-4950.

70.   Dumcenco, D.; *et al*. Large-Area Epitaxial Mono layer MoS2. *ACS Nano* **2015**, *9*, 4611-4620.

71.   Li, X.; Dong, J.; Idrobo, J. C.; Puretzky, A. A.; Rouleau, C. M.; Geohegan, D. B.; Ding, F.; Xiao, K. Edge-Controlled Growth and Etching of Two-Dimensional GaSe Monolayers. *J. Am. Chem. Soc.* **2017**, *139*, 482-491.

72.   Guo, Y.; Wei, X. L.; Shu, J. P.; Liu, B.; Yin, J. B.; Guan, C. R.; Han, Y. X.; Gao, S.; Chen, Q. Charge Trapping at the MoS_2-SiO_2 Interface and Its Effects on the Characteristics of MoS_2 Metal-Oxide-Semiconductor Field Effect Transistors. *Appl. Phys. Lett.* **2015,** *106*, 103109.

73.   Liu, K. H.; *et al.* Evolution of Interlayer Coupling in Twisted Molybdenum Disulfide Bilayers. *Nat. Commun.* **2014**, *5*, 4966.

74.   Wang, S. S.; Rong, Y. M.; Fan, Y.; Pacios, M.; Bhaskaran, H.; He, K.; Warner, J. H. Shape Evolution of Monolayer MoS_2 Crystals Grown by Chemical Vapor Deposition. *Chemistry of Materials* **2014**, *26*, 6371-6379.

75.   Dong, J. C.; Geng, D. C.; Liu, F. N.; Ding, F. Formation of Twinned Graphene Polycrystals. *Angew. Chem.-Int. Edit.* **2019**, *58*, 7723-7727.

76.   Qi, Y.; Zhang, Z. P.; Deng, B.; Zhou, X. B.; Li, Q. C.; Hong, M.; Li, Y. C.; Liu, Z. F.; Zhang, Y. F. Irreparable Defects Produced by the Patching of h-BN Frontiers on Strongly Interacting Re(0001) and Their Electronic Properties. *J. Am. Chem. Soc.* **2017**, *139*, 5849-5856.

77.   Yang, Y.; Fu, Q.; Li, H. B.; Wei, M. M.; Xiao, J. P.; Wei, W.; Bao, X. H. Creating a Nanospace under an h-BN Cover for Adlayer Growth on Nickel(111). *ACS Nano* **2015**, *9*, 11589-11598.

78.   Xu, Z. G.; Tian, H.; Khanaki, A.; Zheng, R. J.; Suja, M.; Liu, J. L. Large-Area Growth of Multi-Layer Hexagonal Boron Nitride on Polished Cobalt Foils by Plasma-Assisted Molecular Beam Epitaxy. *Scientific Reports* **2017**, *7*, 43100.

79.   Lu, G. Y.; Wu, T. R.; Yuan, Q. H.; Wang, H. S.; Wang, H. M.; Ding, F.; Xie, X. M.; Jiang, M. H. Synthesis of Large Single-Crystal Hexagonal Boron Nitride Grains on Cu-Ni Alloy. *Nat. Commun.* **2015**, *6*, 6160.

80.   Lu, G. Y.; et al. Synthesis of High-Quality Graphene and Hexagonal Boron Nitride Monolayer In-Plane Heterostructure on Cu-Ni Alloy. *Adv. Sci.* **2017**, *4*, 1700076.

81.   Bluhm, H.; Havecker, M.; Knop-Gericke, A.; Kiskinova, M.; Schlogl, R.; Salmeron, M. In situ X-Ray Photoelectron Spectroscopy Studies of Gas-Solid Interfaces at Near-Ambient Conditions. *Mrs Bulletin* **2007**, *32*, 1022-1030.

82.   Seah, M. P. Data Compilations-Their Use to Improve Measurement Certainty in Surface-Analysis by AES and XPS. *Surface and Interface Analysis* **1986**, *9*, 85-98.

83.   Shirley, D. A. High-Resolution X-Ray Photoemission Spectrum of the Valence Bands of Gold. *Phys. Rev. B* **1972**, *5*, 4709-4714.

84.   Doniach, S.; Sunjic, M. Many-Electron Singularity in X-Ray Photoemission and X-Ray Line Spectra from Metals. *J. Phys. C: Solid State Phys.* **1970**, *3*, 285-291.

85.   Kresse, G.; Furthmüller, J. Efficient Iterative Schemes for ab initio Total-Energy Calculations Using a Plane-Wave Basis Set. *Phys. Rev. B* **1996**, *54*, 11169-11186.

86.   Kresse, G.; Joubert, D. From Ultrasoft Pseudopotentials to the Projector Augmented-Wave Method. *Phys. Rev. B* **1999**, *59*, 1758-1775.

2314s

2748s

Time

19° 158°

3182s

3616s

0s Time 5229s

5 µm

(TOC)